JOURNAL OF THE MECHANICAL BEHAVIOR OF BIOMEDICAL MATERIALS 29 (2014) 635–654

Available online at www.sciencedirect.com

ScienceDirect

www.elsevier.com/locate/jmbbm

Extremal states of energy of a double-layered thick-walled tube – Application to residually stressed arteries

Tobias Waffenschmidt[a,*], *Andreas Menzel*[a,b]

[a]*Institute of Mechanics, Department of Mechanical Engineering, TU Dortmund, Leonhard-Euler-Str. 5, D-44227 Dortmund, Germany*

[b]*Division of Solid Mechanics, Lund University, P.O. Box 118, SE-22100 Lund, Sweden*

ARTICLE INFO

Article history:
Received 11 March 2013
Received in revised form
11 May 2013
Accepted 16 May 2013
Available online 31 May 2013

Keywords:
Anisotropic biological tissues
Arteries
Residual stresses
Thick-walled tube
Inflation
Energy-minimisation

ABSTRACT

Various biological tissues are designed to optimally support external loads for complex geometries and mechanobiological structures. This results in complex microstructures of such materials. The design of, for instance, (healthy) arteries, which are in the focus of this work, is characterised by a residually stressed fibre-reinforced multi-layered composite with highly non-linear elastic response. The complex interaction of material properties with the geometry and residual stress effects enables the optimal support under different blood pressures, respectively blood flow, within the vessel. The fibres reinforcing the arterial wall, as well as residual stresses present in the vessel, strongly influence its overall behaviour and performance. Turn-over and remodelling processes of the collagenous fibres occurring in the respective layers – either resulting from natural growth phenomena or from artificially induced changes in loading condition such as stent deployment – support the optimisation of the multi-layered composite structure of arteries for the particular loading conditions present in the artery.

Within this contribution, the overall energetic properties of an artery are discussed by means of the inflation, bending and extension of a double-layered cylindrical tube. Different states of residual stresses and different fibre orientations are considered so that, for instance, representative fibre angles that result in extremal states of the total potential energy can be identified. In view of turn-over and remodelling processes, these orientations are considered to constitute preferred directions of fibre alignment. In summary, the main goal of this work is to calculate optimal material, structural and loading parameters by concepts of energy-minimisation. Several numerical studies show that the obtained values – such as the fibre orientations, the residual axial stretch and the opening angle – are in good agreement with respective physiological parameters reported in the literature.

1. Introduction

The investigation of the mechanical behaviour of soft biological tissues, such as arteries, has gained much attention during the last decades; see e.g. Humphrey (2002) for a general overview. Various biological tissues and structures are designed to optimally support external loading, which often results in complex microstructures of these materials. The design of, for instance, healthy arteries is characterised by a residually stressed fibre-reinforced layer-wise orthotropic composite with highly

*Corresponding author. Tel.: +49 231 755 3567; fax: +49 231 755 2688.
E-mail addresses: tobias.waffenschmidt@udo.edu (T. Waffenschmidt), andreas.menzel@udo.edu, andreas.menzel@solid.lth.se (A. Menzel).

1751-6161/$ - see front matter © 2013 Elsevier Ltd. All rights reserved.
http://dx.doi.org/10.1016/j.jmbbm.2013.05.023

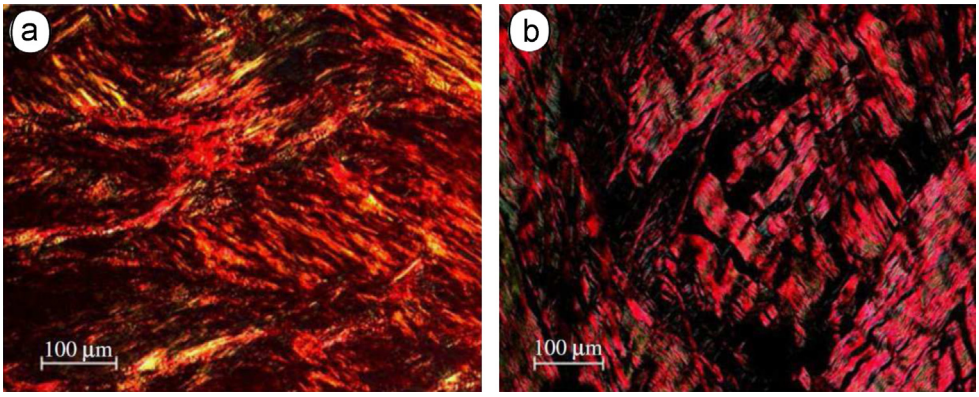

Fig. 1 – Polarised light micrographs of the media (a) and the adventitia (b) of a thoracic aorta wall. The images show two distinct collagen fibre families oriented in the θ–z−plane of the arterial wall. Reprinted from Schriefl et al. (2012), with kind permission from Royal Society Publishing.

nonlinear elastic response. As a result of the interaction between residual stresses and nonlinear anisotropic material properties, arteries may optimally sustain different blood pressures, respectively blood flow, within the vessel. In addition to reducing or rather homogenising the distributions of the respective stress components, the optimal design of the artery e.g. reduces the change in its axial direction under the action of blood flow to a minimum.

Fig. 1 shows two representative micrographs of a thoracic aorta, namely the media (a) and the adventitia (b); the figures are taken from the work by Schriefl et al. (2012). Several advanced constitutive models for the simulation of the mechanical response of arteries have been proposed in the literature and have successfully been applied to realistic patient-specific case studies; see, for instance, the works by Rissland et al. (2009), Holzapfel and Ogden (2010), Balzani et al. (2012) and Creane et al. (2012).

In order to test basic capabilities of the respective constitutive models with application to the simulation of arteries, it is common to analyse an idealised test case, namely the inflation of a thick-walled cylindrical tube. As an advantage, the underlying boundary value problem can be solved (almost) analytically without the need for extensive numerical methods such as the finite element method. Nevertheless, all representative characteristics of the loading conditions and the geometry can be captured; see Holzapfel and Ogden (2003, 2009) and references cited therein. For the present case of application of a residually stressed artery subjected to different blood pressures, commonly combined loading cases including inflation, bending, and axial extension of the thick-walled tube are considered, thereby often neglecting the torsion mode; see the article by Holzapfel et al. (2000) for a particular treatment on arterial wall mechanics. The bending and extension modes are typically related to residual stress states within the arterial wall – which may change in time due to, for instance, ageing effects as discussed in Cardamone et al. (2009) – whereas the inflation refers to loading induced by the blood pressure. Alternative approaches for the inclusion of residual stress states in arteries are discussed in, for instance, Olsson et al. (2006) and Hoger (1985).

The problem of the inflation of a tube is commonly studied by means of hyper-elastic forms together with the underlying equilibrium conditions, respectively the Euler–Lagrange equations; see, for instance, Gent and Rivlin (1952), the monographs by Green and Adkins (1970) as well as Ogden (1997), and the series of papers by Haughton and Ogden (1979, 1980a,b). This allows the investigation of the distribution of stresses under particular loading levels, fibre angles and residual stress states within the multi-layered thick-walled tube; see the contributions by Pipkin and Rivlin (1962) and Spencer et al. (1974), wherein inextensibility of the fibres is assumed. From the mechanical point of view, the fibres reinforce the arterial wall while the residual stresses decrease, e.g. the circumferential stresses within the wall. However, it generally remains unclear which stimulus yields a particular fibre orientation or realignment under changing loading conditions.

Moreover, the interaction of the fibre reorientation with the states of residual stresses shall generally be accounted for; see the work by Alford et al. (2008), wherein the response of an artery in the context of varying properties of the underlying constituents is investigated. Different modelling concepts have been suggested in the literature to simulate the alignment of fibres, commonly denoted as turn-over or remodelling. Particular remodelling formulations are proposed by, for instance, Driessen et al. (2004), where a kinematics-based fibre alignment is suggested, or Humphrey and Rajagopal (2002), wherein a mixture-theory-based remodelling approach is developed. Coaxial states of stresses and strains render the strain energy to take an extremal state, see Sgarra and Vianello (1997), which has motivated alternative remodelling formulation biological tissues with one fibre family, see e.g. Menzel (2005) and Menzel and Waffenschmidt (2009), and two families of fibres, see Menzel (2007). For an overview on different growth and remodelling approaches the reader is referred to the articles by Ambrosi et al. (2011) and Menzel and Kuhl (2012).

Within this contribution, an attempt towards the interpretation of the interactions between loading conditions, states of residual stresses and fibre orientations is made by means of energy-based arguments. As an exemplary constitutive relation, the model proposed by Holzapfel et al. (2000)

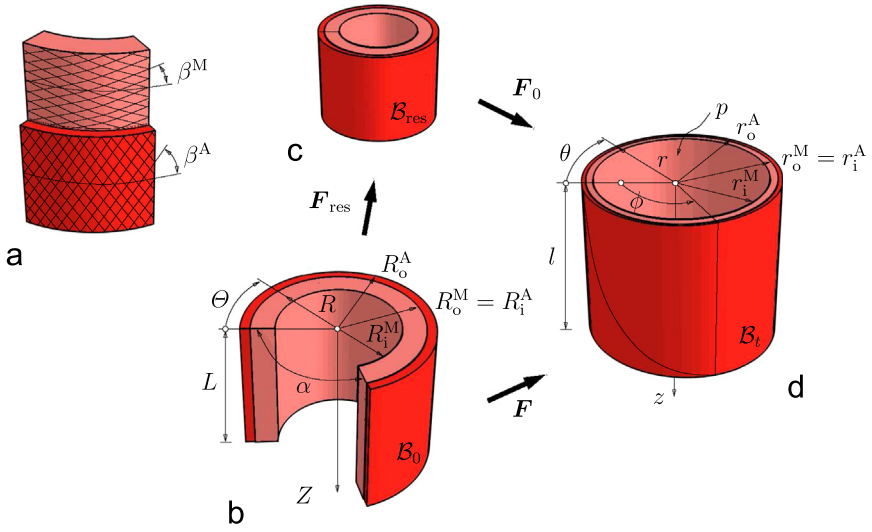

Fig. 2 – Deformation modes of a double-layered thick-walled cylindrical tube, Holzapfel et al. (2000): bending (opening angle α), inflation (internal pressure p), longitudinal extension (axial stretch $\lambda_z = l/L$), and torsion (angle of twist ϕ); (a) segment of the arterial wall consisting of media (superscript M) and adventitia (superscript A) reinforced by two families of fibres with fibre angles β^{M} and β^{A} defined in (b) a stress-free reference configuration $\mathcal{B}_0$; (c) residually stressed but load-free configuration $\mathcal{B}_{\mathrm{res}}$; (d) residually stressed and loaded current configuration $\mathcal{B}_{\mathrm{t}}$.

is adopted and, by analogy with that work, a thick-walled double-layered cylindrical tube subjected to combined bending, inflation and extension is considered. The main goal of the present work is to obtain additional information on optimal, say material, structural and loading parameters – such as the distribution of residual stresses and angles characterising the orientation of fibre families – by direct minimisation concepts applied to the total potential energy of the underlying boundary value problem. In other words, the total potential energy is minimised with respect to one or several primary variables, such as the inner circumferential stretch and a representative fibre angle, to name one example. Thus, results previously established in the literature can be reproduced on the one hand and, as a main goal of this contribution, characteristic settings of material, structural and loading parameters which render the total potential energy to take extremal states can also be investigated on the other. Such extremal states are assumed to identify configurations that, from the design point of view, are favourable.

The present energy-based approach will be restricted to the special case of a perfect cylindrical geometry. Any further geometries accompanied by non-uniform loading cases, as theses intrinsically occur in real patient-specific applications, are beyond the scope of this work but constitute future work in combination with advanced finite element techniques. Moreover, arterial tissue possesses active properties which are not accounted for in this contribution.

Several numerical studies discussed as this work proceeds show that the values calculated for, e.g. the axial residual stretch, the opening angle or the fibre angles, are in good agreement with the respective physiological parameters reported in the literature. As expected, these values correspond to an extremal state of the total potential energy and lead to a reduced, but interestingly not minimal, inner circumferential stretch as compared to the physiological values reported in the literature.

The paper is organised as follows: the analytical expression for the total potential energy for bending, inflation, extension, and torsion of a thick-walled tube is established in Section 2. With this total potential energy function in hand, the Euler–Lagrange equations are derived. Section 3 includes the investigation of characteristic properties of an arterial tube for a specific constitutive model. Several parameter studies are performed by means of a double-layered thick-walled residually stressed tube in response to different loading levels. Finally, the paper concludes with a summary in Section 4.

2. Basic equations of a thick-walled tube

This section reviews the theoretical continuum-mechanical framework applied as this work proceeds. First, basic kinematics of an incompressible thick-walled cylindrical tube, which represents an artery, are addressed in Sections 2.1 and 2.2. The basic modes of deformation discussed are combined bending, inflation, extension and torsion, see Ogden (1997), Holzapfel et al. (2000) or Ogden (2001). Section 2.3 establishes the representation of the total potential energy for the problem at hand and the related Euler–Lagrange equations are summarised in Section 2.4.

2.1. *Basic kinematics*

Position vectors of particles in an undeformed reference configuration $\mathcal{B}_0$ are denoted by $\boldsymbol{X}$ and position vectors in

the deformed current configuration $\mathcal{B}_t$ at time t by $\mathbf{x}=\boldsymbol{\varphi}(\mathbf{X},t)$. The kinematics of a thick-walled tube B can conveniently be described by cylindrical polar coordinates. Adopting common notation, these coordinates are introduced as R, Θ and Z with respect to a chosen reference configuration $\mathcal{B}_0$. An orthonormal referential frame can be defined in terms of these coordinates as

$$\mathbf{E}_R(\Theta)=\cos(\Theta)\mathbf{e}_1+\sin(\Theta)\mathbf{e}_2 \tag{1}$$

$$\mathbf{E}_\Theta(\Theta)=-\sin(\Theta)\mathbf{e}_1+\cos(\Theta)\mathbf{e}_2 \tag{2}$$

$$\mathbf{E}_Z(\Theta)=\mathbf{e}_3 \tag{3}$$

wherein $\{\mathbf{e}_1,\mathbf{e}_2,\mathbf{e}_3\}$ is a Cartesian frame fixed in space. Related coordinates with respect to the current configuration $\mathcal{B}_t$ are introduced as r, θ, z so that the corresponding spatial orthonormal frame reads

$$\mathbf{e}_r(\theta)=\cos(\theta)\mathbf{e}_1+\sin(\theta)\mathbf{e}_2 \tag{4}$$

$$\mathbf{e}_\theta(\theta)=-\sin(\theta)\mathbf{e}_1+\cos(\theta)\mathbf{e}_2 \tag{5}$$

$$\mathbf{e}_z(\theta)=\mathbf{e}_3. \tag{6}$$

The geometry of the tube considered is visualised in Fig. 2 and its material and spatial settings are specified by

$$R_i\le R\le R_o,\quad 0\le\Theta\le 2\pi-\alpha,\quad 0\le Z\le L \tag{7}$$

$$r_i\le r\le r_o,\quad 0\le\theta\le 2\pi,\quad 0\le z\le l, \tag{8}$$

where R_i, R_o and L represent the inner and outer radii and the length of the tube in a (undeformed) reference configuration $\mathcal{B}_0$ while r_i, r_o and l represent the corresponding quantities in the (deformed) current configuration $\mathcal{B}_t$; see Fig. 2. With these quantities in hand, the deformation modes of bending, extension and torsion of an incompressible tube – the deformation due to inflation under internal pressure p will be discussed later on – can be represented by the spatial position vector

$$\mathbf{x}=\boldsymbol{\varphi}(\mathbf{X},t)=r\mathbf{e}_r(\theta)+z\mathbf{e}_z \tag{9}$$

specified by means of

$$r(R)=\sqrt{\frac{R^2-R_i^2}{k\lambda_z}+r_i^2}, \tag{10}$$

$$\theta(\Theta,Z)=k\Theta+Z\frac{\phi}{L}, \tag{11}$$

$$z=\lambda_z Z. \tag{12}$$

The parameter k is defined in terms of the so-called opening angle α, i.e.

$$k=\frac{2\pi}{2\pi-\alpha} \tag{13}$$

as used in Holzapfel et al. (2000), so that $k|_{\alpha=0}=1$ and $k|_{\alpha\to 2\pi}\to\infty$. The positive scalar λ_z represents the axial stretch and ϕ is the angle of twist. Eq. (10) reflects the assumption of incompressibility: for the isochoric deformation of the tube considered the referential sub-volume $V(R)=\pi L[R^2-R_i^2]$ coincides with the current sub-volume $v(r)=\pi l[r^2-r_i^2]$ from which, together with (12), Eq. (10) can be concluded; cf. Ogden (1997, Ch. 2.2.6, pg. 112). The angle θ defined in Eq. (11) is a linear function in Θ, Z and ϕ. In consequence, the radial spatial base vector $\mathbf{e}_r$ does not depend on Θ alone in the case of $\phi\neq 0$.

Representative deformation measures can conveniently be introduced with respect to the coordinates R, Θ, Z and r, θ, z. To set the stage, Eq. (9) is used together with $\nabla_{\mathbf{X}}[\bullet]=\partial_R[\bullet]\otimes\mathbf{E}_R+R^{-1}\partial_\Theta[\bullet]\otimes\mathbf{E}_\Theta+\partial_Z[\bullet]\otimes\mathbf{E}_Z$ – see, e.g. Malvern (1969) – to introduce the deformation gradient $\mathbf{F}=\nabla_{\mathbf{X}}\boldsymbol{\varphi}$ as

$$\mathbf{F}=\nabla_{\mathbf{X}}[r\mathbf{e}_r+z\mathbf{e}_z] \tag{14}$$

$$=\partial_R[r\mathbf{e}_r+z\mathbf{e}_z]\otimes\mathbf{E}_R+\partial_\Theta[r\mathbf{e}_r+z\mathbf{e}_z]\otimes\mathbf{E}_\Theta R^{-1}+\partial_Z[r\mathbf{e}_r+z\mathbf{e}_z]\otimes\mathbf{E}_Z. \tag{15}$$

It is concluded from Eqs. (4)–(6) and (10)–(12) that

$$\frac{\partial\mathbf{e}_r}{\partial R}=\mathbf{0},\quad \frac{\partial\mathbf{e}_r}{\partial\Theta}=\frac{\partial\theta}{\partial\Theta}\mathbf{e}_\theta,\quad \frac{\partial\mathbf{e}_r}{\partial Z}=\frac{\partial\theta}{\partial z}\frac{\partial z}{\partial Z}\mathbf{e}_\theta, \tag{16}$$

whereas $\partial_R\mathbf{e}_z=\partial_\Theta\mathbf{e}_z=\partial_Z\mathbf{e}_z=\mathbf{0}$. Based on Eqs. (10)–(12) and (13) one can specify further partial derivatives, such as

$$\frac{\partial r}{\partial R}=\frac{R}{rk\lambda_z},\quad \frac{\partial z}{\partial Z}=\lambda_z,\quad \frac{\partial\theta}{\partial\Theta}=k,\quad \frac{\partial\theta}{\partial z}=\frac{\phi}{l}, \tag{17}$$

and additionally identify $\partial_\Theta r=\partial_Z r=\partial_R z=\partial_\Theta z=0$. With these relations in hand, the deformation gradient reduces to

$$\mathbf{F}=\frac{R}{rk\lambda_z}\mathbf{e}_r\otimes\mathbf{E}_R+\frac{rk}{R}\mathbf{e}_\theta\otimes\mathbf{E}_\Theta+\lambda_z\mathbf{e}_z\otimes\mathbf{E}_Z+r\frac{\phi}{l}\lambda_z\mathbf{e}_\theta\otimes\mathbf{E}_Z. \tag{18}$$

To simplify notation, common abbreviations are adopted and the radial stretch and a shear measure are introduced as

$$\lambda_r=\frac{R}{rk\lambda_z}\quad\text{and}\quad\gamma=r\frac{\phi}{l}. \tag{19}$$

The incompressibility assumption, i.e. $J=\det(\mathbf{F})=dv/dV=\lambda_r\lambda_\theta\lambda_z\doteq 1$ so that $\mathrm{cof}(\mathbf{F})=\partial_{\mathbf{F}}J=J\mathbf{F}^{-t}$ reduces to $\mathbf{F}^{-t}$, enables us to express the, e.g. circumferential stretch as

$$\lambda_\theta=[\lambda_r\lambda_z]^{-1}=\frac{rk}{R}, \tag{20}$$

so that the deformation gradient, finally, takes the form

$$\mathbf{F}=\lambda_r\mathbf{e}_r\otimes\mathbf{E}_R+\lambda_\theta\mathbf{e}_\theta\otimes\mathbf{E}_\Theta+\lambda_z\mathbf{e}_z\otimes\mathbf{E}_Z+\gamma\lambda_z\mathbf{e}_\theta\otimes\mathbf{E}_Z. \tag{21}$$

It is obvious that the matrix of coefficients of $\mathbf{F}$ is not symmetric in the case of activated twist, i.e. $\gamma\neq 0$, so that λ_r represents a principal stretch in the radial direction, whereas λ_θ and λ_z do not constitute principal stretches. As this work proceeds, however, twist will be neglected so that $\gamma=0$, the matrix of coefficients of $\mathbf{F}$ becomes symmetric and λ_r, λ_θ, λ_z take the interpretation as principal stretches in radial, circumferential and axial direction.

2.2. *Residual stresses*

The incorporation of residual stresses is of key importance within the modelling and simulation of soft biological tissues. Different concepts have been discussed in the literature to account for these equilibrated stress contributions present in the absence of external loading; see, e.g. Hoger (1986) where special emphasis is placed on circular cylinders. In this work a framework discussed by Hoger (1993) and Johnson and Hoger (1995) is adopted which makes use of an additional configuration. The general concept is similar to the introduction of a local isomorphism, as advocated by Noll (1967), but the related energetic contributions are different. Conceptually speaking, one introduces a residual strain quantity which, in combination with a hyper-elastic form specified later on, induces a residual stress contribution.

In this context, let the overall deformation be formally composed as $\boldsymbol{\varphi}=\boldsymbol{\varphi}_0\circ\boldsymbol{\varphi}_{\mathrm{res}}$, where $\boldsymbol{\varphi}_{\mathrm{res}}$ generates a – in general

incompatible – load-free but residually stressed configuration $\mathcal{B}_{\text{res}}$. The mapping $\boldsymbol{\varphi}_0$ accounts for the motion under the action of external forces. For the problem at hand, $\boldsymbol{\varphi}_{\text{res}}$ induces circumferential residual stretches, while $\boldsymbol{\varphi}_0$ will be associated with inflation of the tube and, in general, may also include a torsional deformation mode. Axial elongation may either be attached to $\boldsymbol{\varphi}_{\text{res}}$ or $\boldsymbol{\varphi}_0$. As mentioned above, a twist contribution is neglected as this work proceeds. In view of the overall deformation gradient one obtains the multiplicative composition $\boldsymbol{F}=\boldsymbol{F}_0\cdot\boldsymbol{F}_{\text{res}}$, which is illustrated in Fig. 2; cf. Holzapfel et al. (2000). In terms of the cylindrical coordinates introduced, the respective contributions to the deformation gradient take the representations

$$\boldsymbol{F}_0=\mathrm{R}[r\lambda_z]^{-1}\boldsymbol{e}_r\otimes\boldsymbol{E}_{\mathrm{R}}+r\mathrm{R}^{-1}\boldsymbol{e}_\theta\otimes\boldsymbol{E}_\Theta+\lambda_z\boldsymbol{e}_z\otimes\boldsymbol{E}_Z, \tag{22}$$

$$\boldsymbol{F}_{\text{res}}=k^{-1}\boldsymbol{e}_r\otimes\boldsymbol{E}_{\mathrm{R}}+k\boldsymbol{e}_\theta\otimes\boldsymbol{E}_\Theta+\boldsymbol{e}_z\otimes\boldsymbol{E}_Z, \tag{23}$$

where the entire axial strain is attached to $\boldsymbol{F}_0$. The circumferential residual stretch, described by the opening angle α, must directly be included in $\boldsymbol{F}_{\text{res}}$, whereas an axial residual stretch can either be incorporated in $\boldsymbol{F}_{\text{res}}$ or $\boldsymbol{F}_0$, or can be enforced by Dirichlet boundary conditions. Moreover, note that this composition of the deformation gradient can conveniently be used to model residual stresses within finite element formulations for the simulation of complex boundary value problems; the reader is referred to, e.g, Alastrué et al. (2007, 2009) and references cited in these works.

2.3. Total potential energy

The total potential energy of a conservative system considered additively combines the internal contribution Π_{int}, reflecting the action of internal forces, and an external contribution $\Pi_{\text{ext}}=\Pi^{\text{vol}}_{\text{ext}}+\Pi^{\text{sur}}_{\text{ext}}$ due to the volume and surface forces applied, i.e.

$$\Pi=\Pi_{\text{int}}+\Pi^{\text{vol}}_{\text{ext}}+\Pi^{\text{sur}}_{\text{ext}}+\text{const.} \tag{24}$$

The existence of a strain energy function $\Psi(\boldsymbol{F};\boldsymbol{X})$ is assumed, with the dependency on $\boldsymbol{X}$ often not explicitly mentioned in the following, so that the internal energy contribution of $\mathcal{B}$ can be represented as

$$\Pi_{\text{int}}=\int_{\mathcal{B}_t}J^{-1}\Psi(\boldsymbol{F})\,\mathrm{d}v=\int_{\mathcal{B}_0}\Psi(\boldsymbol{F})\,\mathrm{d}V. \tag{25}$$

In view of the specific application considered as this work proceeds, the volume force contribution is neglected—in other words, $-\partial_{\boldsymbol{\varphi}}\Pi^{\text{vol}}_{\text{ext}}=\boldsymbol{b}\doteq\boldsymbol{0}$ is consistently assumed. Moreover, for the case of pressure loading the traction vector $\boldsymbol{t}$ is proportional to the outward normal unit vector $\boldsymbol{n}$ and its length is referred to the volume-related pressure, i.e. $-\partial_{\boldsymbol{\varphi}}\Pi^{\text{sur}}_{\text{ext}}=\boldsymbol{t}\doteq-p^{\text{vol}}\,\boldsymbol{n}$. Similarly, the referential volume-related traction vector takes the Piola-transformed representation $\overline{\boldsymbol{t}}=-p^{\text{vol}}\ \operatorname{cof}(\boldsymbol{F})\cdot\boldsymbol{N}$, where $\boldsymbol{N}$ is the referential outward unit vector referring to the referential inner surface of the tube $\partial\mathcal{B}_{0\text{i}}$. In case of pressure loading, the referential surface-related energy contribution can be expressed as

$$\tilde{\Pi}^{\text{sur}}_{\text{ext}}=\int_{\partial\mathcal{B}_{0\text{i}}}p^{\text{sur}}\boldsymbol{\varphi}\cdot\operatorname{cof}(\boldsymbol{F})\cdot\boldsymbol{N}\,\mathrm{d}A \tag{26}$$

with $p^{\text{sur}}=\int_0^1 p^{\text{vol}}(\alpha\boldsymbol{v})\alpha^2\,\mathrm{d}\alpha$ being the surface-related pressure for any sufficiently smooth vector function $\boldsymbol{v}$; cf. Podio-Guidugli and Vergara Caffarelli (1990) and Šilhavý (1997, sect. 13). For the loading case considered in the present work, one obtains with regard to Eq. (26) the equivalent volume-related external energy contribution

$$\tilde{\Pi}^{\text{vol}}_{\text{ext}}=-\int_{\mathcal{V}_t}p^{\text{vol}}\mathrm{d}v=-\int_{\mathcal{V}_0}J\,p^{\text{vol}}\,\mathrm{d}V. \tag{27}$$

The equivalence between $\tilde{\Pi}^{\text{sur}}_{\text{ext}}$ and $\tilde{\Pi}^{\text{vol}}_{\text{ext}}$ can be illustrated by relating the surface integral in Eq. (26) to a volume integral by means of Gauss's theorem. To be specific, one obtains

$$\begin{aligned}\tilde{\Pi}^{\text{sur}}_{\text{ext}}&=-\int_{\partial\mathcal{V}_0}p^{\text{sur}}\,\boldsymbol{\varphi}\cdot\operatorname{cof}(\boldsymbol{F})\cdot\boldsymbol{N}\,\mathrm{d}A\\&=-\int_{\mathcal{V}_0}\nabla_{\boldsymbol{X}}\cdot[p^{\text{sur}}\boldsymbol{\varphi}\cdot\operatorname{cof}(\boldsymbol{F})]\,\mathrm{d}V\\&=-\int_{\mathcal{V}_0}p^{\text{sur}}\boldsymbol{F}:\operatorname{cof}(\boldsymbol{F})+\boldsymbol{\varphi}\cdot\operatorname{cof}(\boldsymbol{F})\cdot\nabla_{\boldsymbol{X}}p^{\text{sur}}\,\mathrm{d}V\\&=-\int_{\mathcal{V}_t}3p^{\text{sur}}+\boldsymbol{\varphi}\cdot\nabla_{\boldsymbol{x}}p^{\text{sur}}\,\mathrm{d}v\\&=-\int_{\mathcal{V}_t}p^{\text{vol}}\,\mathrm{d}v=\tilde{\Pi}^{\text{vol}}_{\text{ext}}\end{aligned} \tag{28}$$

wherein use of the Piola identity $\nabla_{\boldsymbol{X}}\cdot\operatorname{cof}(\boldsymbol{F})=\boldsymbol{0}$ has been made; cf. Podio-Guidugli and Vergara Caffarelli (1990).

Note that the change in sign from Eqs. (26)–(28)$_1$ refers to the change in direction of the outward normal vectors related to the inner lateral surface of the tube, $\partial\mathcal{B}_{0\text{i}}$, and the surface of the inner volume of the tube, $\partial\mathcal{V}_0$. Furthermore, it becomes apparent that the relation between p^{sur} and p^{vol} is in line with the definition mentioned above, and as a special case, i.e. if $\nabla_{\boldsymbol{x}}p^{\text{sur}}=\boldsymbol{0}$, one observes the relation $p^{\text{sur}}=\frac{1}{3}p^{\text{vol}}$. An alternative derivation based on the introduction of $\boldsymbol{n}$ in terms of the vector product of two surface tangent vectors is included in, e.g. Bonet and Wood (1997, chap. 6).

Summarising the total potential energy for the tube problem at hand and making use of the coordinates and deformation measures introduced above, one obtains

$$\begin{aligned}\Pi=&\int_{z=0}^{l}\int_{\theta=0}^{2\pi}\int_{r=r_{\text{i}}}^{r_{\text{o}}}\tilde{\Psi}(\lambda_\theta(r),\lambda_z))r\,\mathrm{d}r\,\mathrm{d}\theta\,\mathrm{d}z\\&-\int_{z=0}^{l}\int_{\theta=0}^{2\pi}\int_{r=0}^{r_{\text{i}}}pr\,\mathrm{d}r\,\mathrm{d}\theta\,\mathrm{d}z+\text{const.}\\=&\,2\pi\,l\int_{r=r_{\text{i}}}^{r_{\text{o}}}\tilde{\Psi}(\lambda_\theta(r),\lambda_z)r\,\mathrm{d}r-p\pi r_{\text{i}}^2 l+\text{const},\end{aligned} \tag{29}$$

wherein it is assumed that the internal energy density can be expressed as a function of the principal stretches and the incompressibility constraint has been accounted for. Moreover, external contributions acting on the outer surface boundary are assumed to vanish identically. The volume-related pressure is homogeneously distributed within $\mathcal{V}_t$, so that $\nabla_{\boldsymbol{x}}p^{\text{vol}}=\boldsymbol{0}$, for the inflation of the thick-walled tube addressed in this work. Moreover, the notation is simplified by the abbreviation $p=p^{\text{vol}}$.

Due to the non-linear dependency of $\tilde{\Psi}$ on r, the integral expression in Eq. (29) can in general not be evaluated analytically. A possible numerical integration scheme will be discussed in Section 3.

2.4. Euler–Lagrange equations

In order to derive the Euler–Lagrange equations, i.e. the equations off equilibrium, the variation of the total potential

energy is calculated to identify stationary points of $\Pi(\mathbf{F},\boldsymbol{\varphi})$. Starting with the representation of the total potential energy with respect to referential volumes and surfaces and assuming dead traction loading on the outer boundary, one obtains the following relations

$$\delta\Pi|_{\mathrm{X}} = \delta\int_{\mathcal{B}_0}\Psi\,\mathrm{dV} - \delta\int_{\mathcal{V}_0} pJ\,\mathrm{dV} - \delta\int_{\partial\mathcal{B}_{0\mathrm{o}}}\boldsymbol{\varphi}\cdot\bar{\mathbf{t}}_{\mathrm{o}}\,\mathrm{dA} \tag{30}$$

$$= \int_{\mathcal{B}_0}\partial_{\mathbf{F}}\Psi : \nabla_{\mathrm{X}}\delta\boldsymbol{\varphi}\,\mathrm{dV} - \int_{\mathcal{V}_0} J\partial_{\boldsymbol{\varphi}}p\cdot\delta\boldsymbol{\varphi} + p\,\mathrm{cof}(\mathbf{F}) : \nabla_{\mathrm{X}}\delta\boldsymbol{\varphi}\,\mathrm{dV} - \int_{\partial\mathcal{B}_{0\mathrm{o}}}\delta\boldsymbol{\varphi}\cdot\bar{\mathbf{t}}_{\mathrm{o}}\,\mathrm{dA} \tag{31}$$

$$= \int_{\mathcal{B}_0}\nabla_{\mathrm{X}}\cdot[\delta\boldsymbol{\varphi}\cdot\partial_{\mathbf{F}}\Psi] - \delta\boldsymbol{\varphi}\cdot[\nabla_{\mathrm{X}}\cdot\partial_{\mathbf{F}}\Psi]\,\mathrm{dV} - \int_{\mathcal{V}_0} J\partial_{\boldsymbol{\varphi}}p\cdot\delta\boldsymbol{\varphi} + p\nabla_{\mathrm{X}}\cdot[\delta\boldsymbol{\varphi}\cdot\mathrm{cof}(\mathbf{F})]\,\mathrm{dV} - \int_{\partial\mathcal{B}_{0\mathrm{o}}}\delta\boldsymbol{\varphi}\cdot\bar{\mathbf{t}}_{\mathrm{o}}\,\mathrm{dA} \tag{32}$$

$$= \int_{\partial\mathcal{B}_0}\delta\boldsymbol{\varphi}\cdot\partial_{\mathbf{F}}\Psi\cdot\mathbf{N}\,\mathrm{dA} - \int_{\mathcal{B}_0}\delta\boldsymbol{\varphi}\cdot[\nabla_{\mathrm{X}}\cdot\partial_{\mathbf{F}}\Psi]\,\mathrm{dV} - \int_{\mathcal{V}_0}\nabla\mathbf{X}\cdot[p\delta\boldsymbol{\varphi}\cdot\mathrm{cof}(\mathbf{F})]\,\mathrm{dV} - \int_{\partial\mathcal{B}_{0\mathrm{o}}}\delta\boldsymbol{\varphi}\cdot\bar{\mathbf{t}}_{\mathrm{o}}\,\mathrm{dA} \tag{33}$$

$$= \int_{\partial\mathcal{B}_0}\delta\boldsymbol{\varphi}\cdot\mathbf{P}\cdot\mathbf{N}\,\mathrm{dA} - \int_{\mathcal{B}_0}\delta\boldsymbol{\varphi}\cdot[\nabla_{\mathrm{X}}\cdot\mathbf{P}]\,\mathrm{dV} - \int_{\mathcal{V}_0} p\,\delta\boldsymbol{\varphi}\cdot\mathrm{cof}(\mathbf{F})\cdot\mathbf{N}\,\mathrm{dA} - \int_{\partial\mathcal{B}_{0\mathrm{o}}}\delta\boldsymbol{\varphi}\cdot\bar{\mathbf{t}}_{\mathrm{o}}\,\mathrm{dA}\doteq 0, \tag{34}$$

wherein Gauss's theorem, the Piola identity and $J\partial_{\boldsymbol{\varphi}}p = \mathrm{cof}(\mathbf{F})\cdot\nabla_{\mathrm{X}}p$ have been applied; cf. Podio-Guidugli and Vergara Caffarelli (1990) and Haughton (2001). Moreover, the Piola stresses are introduced as $\mathbf{P} = \partial_{\mathbf{F}}\Psi$ and the traction vector prescribed at the outer boundary $\partial\mathcal{B}_{0\mathrm{o}}$ is denoted as $\bar{\mathbf{t}}_{\mathrm{o}}\doteq$const. Based on this, the local Euler–Lagrange equations take the representation

$$\mathbf{0} = \nabla_{\mathrm{X}}\cdot\mathbf{P} \qquad \text{in } \mathcal{B}_0 \tag{35}$$

$$\bar{\mathbf{t}} = \mathbf{P}\cdot\mathbf{N} = \bar{\mathbf{t}}_{\mathrm{o}} \qquad \text{on } \partial\mathcal{B}_{0\mathrm{o}} \tag{36}$$

$$\bar{\mathbf{t}} = \mathbf{P}\cdot\mathbf{N} = -p\,\mathrm{cof}(\mathbf{F})\cdot\mathbf{N} \qquad \text{on } \partial\mathcal{B}_{0\mathrm{i}}. \tag{37}$$

As indicated above, the referential outward normals $\mathbf{N}$ in the first and third term of Eq. (34) refer to differently oriented surfaces, namely the surface of tube $\partial\mathcal{B}_0$ and the surface of the inner volume of the tube $\partial\mathcal{V}_0$, respectively. Consequently, a change in sign from the third term in Eqs. (34)–(37) is considered. By analogy with Eq. (29), the Piola stresses are next assumed to take a spectral form with respect to the base systems introduced in Eqs. (1)–(6), namely $\mathbf{P} = P_{rR}\mathbf{e}_r\otimes\mathbf{E}_R + P_{\theta\Theta}\mathbf{e}_\theta\otimes\mathbf{E}_\Theta + P_{zZ}\mathbf{e}_z\otimes\mathbf{E}_Z$. Note that this form, together with Eq. (21) and $\gamma\doteq 0$, includes coaxiality of conjugated stresses and strain measures which, however, does not generally restrict the underlying constitutive relation to isotropy. With this assumption in hand and $\mathbf{N} = \pm\mathbf{E}_R$ for the particular application considered, the Euler–Lagrange equations can be represented as

$$\mathbf{0} = \left[\frac{\partial P_{rR}}{\partial R} + \frac{P_{rR}}{R} - \frac{P_{\theta\Theta}}{R}\right]\mathbf{e}_r + \frac{1}{R}\frac{\partial P_{\theta\Theta}}{\partial\Theta}\mathbf{e}_\theta + \frac{\partial P_{zZ}}{\partial Z}\mathbf{e}_z \quad \text{in } \mathcal{B}_0 \tag{38}$$

$$\bar{\mathbf{t}} = P_{rR}\mathbf{e}_r \quad \text{on } \partial\mathcal{B}_0 \tag{39}$$

$$\bar{\mathbf{t}} = p\lambda_r^{-1}\mathbf{e}_r \quad \text{on } \partial\mathcal{B}_{0\mathrm{i}} \tag{40}$$

Instead of choosing representations in terms of the Piola stresses $\mathbf{P}$, which refer to referential area elements, the Euler–Lagrange equations can be formulated in terms of the Cauchy stresses $\boldsymbol{\sigma} = \mathbf{P}\cdot\mathrm{cof}(\mathbf{F}^{-1})$, which refer to spatial area elements. Making use of the Piola identity, the variation of the total potential can be rewritten as

$$\delta\Pi|_{\mathrm{X}} = \int_{\partial\mathcal{B}_{\mathrm{t}}}\delta\boldsymbol{\varphi}\cdot\boldsymbol{\sigma}\cdot\boldsymbol{n}\,\mathrm{da} - \int_{\mathcal{B}_{\mathrm{t}}}\delta\boldsymbol{\varphi}\cdot[\nabla_{\mathrm{x}}\cdot\boldsymbol{\sigma}]\,\mathrm{dv} - \int_{\partial\mathcal{V}_{\mathrm{t}}} p\delta\boldsymbol{\varphi}\cdot\boldsymbol{n}\,\mathrm{da} - \int_{\partial\mathcal{B}_{\mathrm{o}}}\delta\boldsymbol{\varphi}\cdot\mathbf{t}_{\mathrm{o}}\,\mathrm{da}\doteq 0. \tag{41}$$

Based on this, the Euler–Lagrange equation in terms of spatial arguments take the representation

$$\mathbf{0} = \nabla\mathbf{x}\cdot\boldsymbol{\sigma} \qquad \text{in } \mathcal{B}_{\mathrm{t}} \tag{42}$$

$$\mathbf{t} = \boldsymbol{\sigma}\cdot\boldsymbol{n} = \mathbf{t}_{\mathrm{o}} \qquad \text{on } \partial\mathcal{B}_{\mathrm{to}} \tag{43}$$

$$\mathbf{t} = \boldsymbol{\sigma}\cdot\boldsymbol{n} = -p\boldsymbol{n} \qquad \text{on } \partial\mathcal{B}_{\mathrm{ti}} \tag{44}$$

In view of the base system introduced in Eqs. (4)–(6), together with the assumed coaxiality of conjugated stresses and strain measures, the Cauchy stresses allow representation in spectral form as $\boldsymbol{\sigma} = \sigma_{rr}\mathbf{e}_r\otimes\mathbf{e}_r + \sigma_{\theta\theta}\mathbf{e}_\theta\otimes\mathbf{e}_\theta + \sigma_{zz}\mathbf{e}_z\otimes\mathbf{e}_z$. By analogy with the derivations reviewed above and with $\boldsymbol{n} = \pm\mathbf{e}_r$, the Euler–Lagrange equations can be summarised as

$$\mathbf{0} = \left[\frac{\partial\sigma_{rr}}{\partial r} + \frac{\sigma_{rr}}{r} - \frac{\sigma_{\theta\theta}}{r}\right]\mathbf{e}_r + \frac{1}{r}\frac{\partial\sigma_{\theta\theta}}{\partial\theta}\mathbf{e}_\theta + \frac{\partial\sigma_{zz}}{\partial z}\mathbf{e}_z \quad \text{in } \mathcal{B}_{\mathrm{t}} \tag{45}$$

$$\mathbf{t} = \sigma_{rr}\mathbf{e}_r \qquad \text{on } \partial\mathcal{B}_{\mathrm{to}} \tag{46}$$

$$\mathbf{t} = p\mathbf{e}_r \qquad \text{on } \partial\mathcal{B}_{\mathrm{ti}} \tag{47}$$

In summary, stationary points of $\Pi(\mathbf{F},\boldsymbol{\varphi})$ for the rotationally symmetric inflation of a thick-walled tube can be represented with respect to the base systems in (1)–(6) as

$$\delta\Pi|_{\mathrm{X}} = \int_{\partial\mathcal{B}_0}\delta\varphi_r P_{rR}R\,\mathrm{d}\Theta\,\mathrm{dZ} - \int_{\mathcal{B}_0}\left[\delta\varphi_r\left[\frac{\partial[RP_{rR}]}{\partial R} - P_{\theta\Theta}\right] + \delta\varphi_\theta\frac{\partial P_{\theta\Theta}}{\partial\Theta} + \delta\varphi_z\frac{\partial[RP_{zZ}]}{\partial Z}\right]\mathrm{dR}\,\mathrm{d}\Theta\,\mathrm{dZ} - \int_{\partial\mathcal{B}_{\mathrm{ti}}}\delta\varphi_r p\lambda_r^{-1}R\,\mathrm{d}\Theta\,\mathrm{dZ} - \int_{\partial\mathcal{B}_{0\mathrm{o}}}\delta\varphi_r\,\bar{\mathrm{t}}_r R\,\mathrm{d}\Theta\,\mathrm{dZ} \tag{48}$$

$$= \int_{\partial\mathcal{B}_{\mathrm{t}}}\delta\varphi_r\sigma_{rr}r\,\mathrm{d}\theta\,\mathrm{dz} - \int_{\mathcal{B}_{\mathrm{t}}}\left[\delta\varphi_r\left[\frac{\partial[r\sigma_{rr}]}{\partial r} - \sigma_{\theta\theta}\right] + \delta\varphi_\theta\frac{\partial\sigma_{\theta\theta}}{\partial\theta} + \delta\varphi_z\frac{\partial[r\sigma_{zz}]}{\partial z}\right]\mathrm{dr}\,\mathrm{d}\theta\,\mathrm{dz} - \int_{\partial\mathcal{B}_{\mathrm{ti}}}\delta\varphi_r pr\,\mathrm{d}\theta\,\mathrm{dz} - \int_{\partial\mathcal{B}_{\mathrm{to}}}\delta\varphi_r t_r r\,\mathrm{d}\theta\,\mathrm{dz}\doteq 0 \tag{49}$$

with $\delta\boldsymbol{\varphi} = \delta\varphi_r\mathbf{e}_r + \delta\varphi_\theta\mathbf{e}_\theta + \delta\varphi_z\mathbf{e}_z$. As this work proceeds, $P_{rR} = 0$ on $\partial\mathcal{B}_{0\mathrm{o}}$ is assumed, respectively $\sigma_{rr} = 0$ on $\partial\mathcal{B}_{\mathrm{to}}$, but the tube could also interact with the ambient space such that the radial stresses do not vanish identically on the outer surface boundary. Note that in case of shear stresses being activated at the outer surface boundary, the stresses do not remain

coaxial with respect to conjugated strain measures for the constitutive relations considered later on.

3. Analysis of a double-layered thick-walled tube

The structural response of a thick-walled double-layered arterial tube subjected to combined bending, inflation and extension is investigated by means of minimising the total potential energy functional (29). Several multivariable optimisation problems with respect to combinations of up to five variables of loading-type and structure-type are set up and solved. The computational results are discussed and compared to physiological values taken from the literature.

3.1. Constitutive model

To set the stage, the underlying constitutive model adopted for the following investigations is briefly reviewed. To be specific, use of an orthotropic model with two families of fibres is made as introduced by Holzapfel et al. (2000); for a general review on the modelling of fibre reinforced materials the reader is also referred to Spencer (1972) and the contributions in Spencer (1984) and Boehler (1987). The strain energy density of this model is assumed to additively decompose into an isotropic part $\Psi^{\mathrm{n}}_{\mathrm{iso}}$, representing the contribution of the non-collagenous ground material, and an anisotropic part $\Psi^{\mathrm{n}}_{\mathrm{ani}}$, representing the contributions of the different families of collagen fibres, i.e.

$$\Psi^{\mathrm{n}}(\boldsymbol{F}, \boldsymbol{a}^{\mathrm{n}}_{0\ 1,\dots,N}) = \Psi^{\mathrm{n}}_{\mathrm{iso}}(\boldsymbol{F}) + \Psi^{\mathrm{n}}_{\mathrm{ani}}(\boldsymbol{F}, \boldsymbol{a}^{\mathrm{n}}_{0\ 1,\dots,N}), \tag{50}$$

wherein $\mathrm{n} = \mathrm{M}$ represents the media and $\mathrm{n} = \mathrm{A}$ the adventitia. Moreover, $\boldsymbol{a}_{0\ 1,\dots,N}$ denotes a set of N referential unit-vectors characterising the fibre families considered. The isotropic part of the strain energy is specified by a common neo-Hookean format

$$\Psi^{\mathrm{n}}_{\mathrm{iso}}(\boldsymbol{F}) = \frac{c^{\mathrm{n}}}{2}[I_1 - 3], \tag{51}$$

with

$$I_1 = \boldsymbol{F} : \boldsymbol{F} = \lambda_\theta^2 + \lambda_z^2 + \lambda_\theta^{-2}\lambda_z^{-2} \tag{52}$$

for $J \doteq 1$. The anisotropic part adopted takes the following exponential form:

$$\Psi^{\mathrm{n}}_{\mathrm{ani}}(\boldsymbol{F}, \boldsymbol{a}^{\mathrm{n}}_{0\ 1,\dots,N}) = \frac{k^{\mathrm{n}}_1}{2k^{\mathrm{n}}_2} \sum_{\mathrm{i}=1}^{N} [\exp(k^{\mathrm{n}}_2 \langle E^{\mathrm{n}}_{\mathrm{i}} \rangle^2) - 1], \tag{53}$$

wherein it is assumed that the fibres within each layer n are mechanically equivalent. The notation $\langle \bullet \rangle = [|\bullet| + \bullet]/2$ reflects the Macaulay brackets. These allow activation of the fibre contributions in the tension regime only. To be specific, the referential strain measure $E^{\mathrm{n}}_{\mathrm{i}}$ is introduced as

$$E^{\mathrm{n}}_{\mathrm{i}} = \boldsymbol{a}^{\mathrm{n}}_{0\mathrm{i}} \cdot \boldsymbol{F}^{\mathrm{t}} \cdot \boldsymbol{F} \cdot \boldsymbol{a}^{\mathrm{n}}_{0\mathrm{i}} - 1 = I^{\mathrm{n}}_{4\mathrm{i}} - 1. \tag{54}$$

Even though Eq. (54) does not include any dispersion of fibre contributions, the formulation can be extended to account for these as discussed in, for instance, Gasser et al. (2006) and Menzel et al. (2008). As this work proceeds, the number of mechanically equivalent fibre families per layer is restricted to $N = 2$ and, moreover, their initial orientations are assumed as

$$\boldsymbol{a}^{\mathrm{n}}_{0\ 1,2} = \sin(\beta^{\mathrm{n}})\boldsymbol{E}_Z \pm \cos(\beta^{\mathrm{n}})\boldsymbol{E}_\theta, \tag{55}$$

see the graphical illustration in Fig. 2. This kinematic relation together with Eq. (21) and $\gamma = 0$ renders stresses and conjugated strain measures to be coaxial. Furthermore, one observes $E^{\mathrm{n}}_1 = E^{\mathrm{n}}_2 \doteq E^{\mathrm{n}}$ and the invariant introduced in Eq. (54) can be expressed as

$$I^{\mathrm{n}}_{4\mathrm{i}} = \boldsymbol{a}^{\mathrm{n}}_{0\mathrm{i}} \cdot \boldsymbol{F}^{\mathrm{t}} \cdot \boldsymbol{F} \cdot \boldsymbol{a}^{\mathrm{n}}_{0\mathrm{i}} = \sin^2(\beta^{\mathrm{n}})\lambda_z^2 + \cos^2(\beta^{\mathrm{n}})\lambda_\theta^2. \tag{56}$$

In conclusion, the strain energy can be written as a function in terms of the circumferential and longitudinal stretch, i.e. $\tilde{\Psi}^{\mathrm{n}}(\lambda_\theta, \lambda_z)$, as indicated in Eq. (29).

With these relations in hand, the Cauchy stress tensor $\boldsymbol{\sigma}^{\mathrm{n}} = \partial_{\boldsymbol{F}} \Psi^{\mathrm{n}} \cdot \mathrm{cof}(\boldsymbol{F}^{-1})$ can be specified, namely

$$\boldsymbol{\sigma}^{\mathrm{n}} = c^{\mathrm{n}}\, \boldsymbol{F} \cdot \boldsymbol{F}^{\mathrm{t}} + 4k^{\mathrm{n}}_1 E^{\mathrm{n}} \exp(k_2 \langle E^{\mathrm{n}} \rangle^2)[\boldsymbol{a}^{\mathrm{n}}_1 \otimes \boldsymbol{a}^{\mathrm{n}}_1 + \boldsymbol{a}^{\mathrm{n}}_2 \otimes \boldsymbol{a}^{\mathrm{n}}_2] \tag{57}$$

with $\boldsymbol{a}^{\mathrm{n}}_{1,2} = \boldsymbol{F} \cdot \boldsymbol{a}^{\mathrm{n}}_{01,2}$. Alternatively, the Cauchy stress tensor can be expressed with respect to the base system introduced in Eqs. (4)–(6), or rather in spectral form, as

$$\sigma^{\mathrm{n}}_{rr} = c^{\mathrm{n}} \lambda_\theta^{-2} \lambda_z^{-2} \tag{58}$$

$$\sigma^{\mathrm{n}}_{\theta\theta} = c^{\mathrm{n}} \lambda_\theta^2 + 4\, \cos^2(\beta^{\mathrm{n}}) k^{\mathrm{n}}_1 \lambda_\theta^2 E^{\mathrm{n}} \exp(k^{\mathrm{n}}_2 \langle E^{\mathrm{n}} \rangle^2) \tag{59}$$

Table 1 – Material, structural and geometrical parameters for a carotid artery of a rabbit adopted from Holzapfel et al. (2000), respectively Chuong and Fung (1983). The index $\mathrm{n} = \mathrm{M}$ refers to the media, whereas $\mathrm{n} = \mathrm{A}$ refers to the adventitia. This parameter set is used throughout if not otherwise stated. Note that the inner referential radii $\mathrm{R}^{\mathrm{n}}_{\mathrm{i}}$ are assumed to linearly depend on the opening angle α; cf. Eq. (61).

Type	Parameter	Description	Value		Unit
			Media (n = M)	Adventitia (n = A)	
Material	c^{n}	Elastic constant	3.0	0.3	[kPa]
	k^{n}_1	Elastic constant	2.3632	0.5620	[kPa]
	k^{n}_2	Elastic constant	0.8393	0.7112	[–]
Structural	β^{n}	Fibre angle	29.0	62.0	[deg]
Geometrical	H^{n}	Referential wall thickness	0.26	0.13	[mm]
	$L^{\mathrm{n}} = R^{\mathrm{M}}_{\mathrm{i}}\|_{\alpha=0^\circ}$	Referential length	0.71	0.71	[mm]
	$R^{\mathrm{n}}_{\mathrm{i}}\|_{\alpha=0^\circ}$	Inner referential radius	0.71	0.97	[mm]
	$R^{\mathrm{n}}_{\mathrm{o}}\|_{\alpha=0^\circ}$	Outer referential radius	0.97	1.1	[mm]
	$R^{\mathrm{n}}_{\mathrm{i}}\|_{\alpha=160^\circ}$	Inner referential radius	1.43	1.69	[mm]
	$R^{\mathrm{n}}_{\mathrm{o}}\|_{\alpha=160^\circ}$	Outer referential radius	1.69	1.82	[mm]

$$\sigma_{zz}^{n} = c^{n}\lambda_z^2 + 4\,\sin^2(\beta^{n})k_1^{n}\lambda_z^2 E^{n}\exp(k_2^{n}\langle E^{n}\rangle^2) \tag{60}$$

Even though not highlighted, the Piola stresses can be represented by analogy with Eqs. (57)–(60).

3.2. *Material, structural and geometrical parameters*

For reasons of comparability, the material, structural and geometrical parameters used in this contribution are adopted from Holzapfel et al. (2000) as originally identified by Chuong and Fung (1983); see Table 1. Note that in Holzapfel et al. (2000) the inner referential radii R_i^{n} are assumed to depend on the opening angle α. For the subsequent studies, where different opening angles α are considered, the inner referential radius R_i^{M} is linearly interpolated by means of

$$R_i^{M}(\alpha) = \frac{R_i^{M}|_{\alpha=160} - R_i^{M}|_{\alpha=0}}{160}\alpha + R_i^{M}|_{\alpha=0} \tag{61}$$

depending on the actual value of α, here included in unit-free form.

For illustration and comparison purposes, contour plots of the strain energy density (50) for the media and adventitia based on the parameters summarised in Table 1 are depicted in Fig. 3; cf. Holzapfel et al. (2000). According to the constitutive assumption that only the ground substance contributes in case of compressive loading, one observes an isotropic behaviour in the in-plane compression range, i.e. for $\lambda_\theta<1$ and $\lambda_z<1$, which is reflected by the symmetric contour lines within this region. In contrast, for in-plane tensile loading, i.e. $\lambda_\theta>1$ and $\lambda_z>1$, the collagen fibres essentially affect the constitutive behaviour, and one consequently obtains an anisotropic response. In this regard, one observes that the directions of largest ascent are essentially different for the media and adventitia, see Fig. 2(a).

3.3. *Loading parameters*

In the following, parameters essentially affecting the deformation of the specimen are referred to as loading parameters. The loading parameters used in this contribution are adopted from Holzapfel et al. (2000) and summarised in Table 2. For later evaluation and comparison, the physiological inner circumferential stretch $\lambda_{\theta i}^{phys}$ corresponding to the physiological values in Table 2 can be computed by means of the relation

$$\lambda_{\theta i}^{phys} = \frac{kr_i}{R_i}. \tag{62}$$

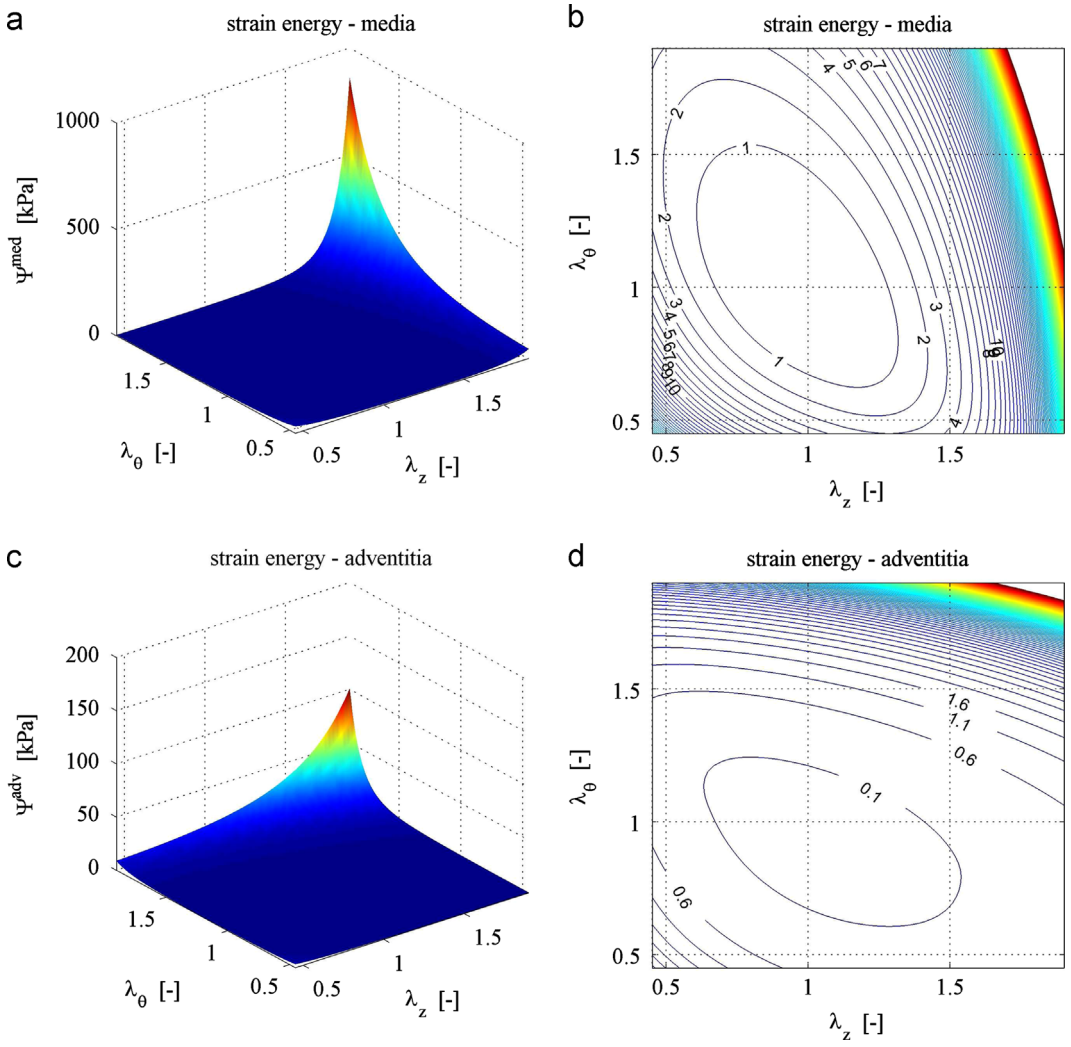

Fig. 3 – Contour plots of the strain energy density (50) for the media (a, b) and for the adventitia (c, d) based on the material parameters given in Table 1.

Table 2 – Loading parameters included in the total potential energy (29). The pressure p directly enters the external potential energy, see Eq. (29), whereas the axial stretch λ_z and the opening angle α are included in the internal potential energy via the deformation gradient $\boldsymbol{F}$, see Eq. (21). The physiological values are adopted from Holzapfel et al. (2000) and correspond to an inner circumferential stretch of $\lambda_{\theta i}^{\text{phys}} = 1.604$, see Eq. (62). The discrete pressure values are related to the systolic blood pressure $p = 17.4$ [kPa], the diastolic blood pressure $p = 8.0$ [kPa] and the mean blood pressure $p = 13.33$ [kPa].

Parameter	Description	Load case	Physiological value	Value range		Unit
				Continuous	Discrete	
p	Internal pressure	Inflation	$p^{\text{phys}} = 13.33$	0.0–21.33	[8.0, 13.33, 17.4]	[kPa]
λ_z	Axial stretch	Elongation	$\lambda_z^{\text{phys}} = 1.7$	0.2–1.9	[0.2, 1.0, 1.9]	[–]
α	Opening angle	Bending	$\alpha^{\text{phys}} = 160.0$	0.0–160.0	[0.0, 80.0, 160.0]	[deg]

Table 3 – Algorithm to minimise $\Pi(\lambda_{\theta i}, \lambda_z \doteq \text{const}; \lambda_{\theta i}^0, \boldsymbol{\kappa})$ as given in Eq. (29).

1. Set up material, structural and geometrical parameters from Table 1 for media, n = M, and adventitia, n = A, as well as loading parameters from Table 2 and collect these in pseudo-vector $\boldsymbol{\kappa}$
2. Perform initial guess $\lambda_{\theta i}^0$ for the primary variable, which is the inner circumferential stretch
3. Compute argument of minimum of total energy (29)
   $\lambda_{\theta i}^{\min} = \arg\min_{\lambda_{\theta i}} \Pi(\lambda_{\theta i}, \lambda_z \doteq \text{const}; \lambda_{\theta i}^0, \boldsymbol{\kappa})$,
   wherein Π is determined by the algorithm given in Table 4 – the minimisation can be performed by, e.g. the Matlab `fmincon`-optimisation-function

For $\alpha = 160$ [kPa], $r_i = 1.274$ [mm] and $R_i = 1.43$ [mm] this results in a value of $\lambda_{\theta i}^{\text{phys}} = 1.604$.

3.4. *Algorithmic treatment*

The solution of the underlying boundary value problem is obtained by means of the minimisation of the related total potential energy functional (29), i.e.

$$\lambda_{\theta i}^{\min} = \arg\min_{\lambda_{\theta i}} \Pi(\lambda_{\theta i}, \lambda_z \doteq \text{const}; \lambda_{\theta i}^0, \boldsymbol{\kappa}), \tag{63}$$

with respect to the primary variable $\lambda_{\theta i}$ using an initial guess $\lambda_{\theta i}^0$ and a pseudo-vector $\boldsymbol{\kappa}$ which summarises the material, structural and geometrical parameters as well as the loading parameters.

Such minimisation problems may conveniently be solved by typical optimisation techniques available in commercial software packages used for numerical calculations as, e.g. Matlab. In this study, the Matlab optimisation-algorithm `fmincon` is used which is based on a sequential quadratic programming (SQP) method. Without discussing specific algorithmic details at this stage, this algorithm allows us to find a constrained minimum of a scalar function of one or more variables, whereby initial estimate values must be set. For detailed background information on such constrained nonlinear optimisation problems, the reader is referred to the monographs by Luenberger (1984), Bertsekas (1996) and Dennis and Schnabel (1996).

Solving the aforementioned minimisation problem (63) for the single primary variable $\lambda_{\theta i}$, see Tables 3 and 4, is equivalent to solving the corresponding Euler Lagrange equations in form of Eqs. (35)–(37) or Eqs. (42)–(44). In addition to minimising Π with respect to $\lambda_{\theta i}$, one could also think of solving for extrema of the total or internal potential energy functional with respect to the loading parameters or structural parameters or combinations thereof. In the following, settings of structural or loading parameters, which lead to stationary points of the total or internal potential energy in states of equilibrium, are calculated and it is discussed whether such extremal states of energy can be referred to an optimal or rather natural design of arterial walls.

In view of the algorithm implemented, it is important to note that those problems involving the fibre angles β^{n} as variable quantities rely on a modified computational strategy: the minimisation is first performed for those variables not related to the fibre angles β^{n}, then followed by a maximisation with respect to the fibre angles β^{n}. Alternatively, one could also think of minimising the energy with respect to β^{n}. The physical interpretation of an adaptive biological tissue suggests, however, that its loading capacity is maximised so that the internal energy is maximised in the case of Dirichlet boundary conditions. To give an example, the optimisation in the present context can be understood as

$$\{\beta^{\text{M opt}}, \beta^{\text{A opt}}\} = \arg\operatorname*{opt}_{\beta^{\text{M}}, \beta^{\text{A}}; \lambda_{\theta i}, \lambda_z, \alpha} \Pi^*(\lambda_{\theta i}, \lambda_z, \alpha, \beta^{\text{M}}, \beta^{\text{A}}; \boldsymbol{\kappa}^*) \tag{64}$$

$$= \arg\max_{\beta^{\text{M}}, \beta^{\text{A}}} \left\{ \min_{\lambda_{\theta i}, \lambda_z, \alpha} \Pi^*(\lambda_{\theta i}, \lambda_z, \alpha, \beta^{\text{M}}, \beta^{\text{A}}; \boldsymbol{\kappa}^*) \right\}. \tag{65}$$

In other words, the total potential energy Π is first minimised with respect to variables $\{\lambda_{\theta i}, \lambda_z, \alpha\}$, which results in the quadruple $\{\lambda_{\theta i}^{\min}, \lambda_z^{\min}, \alpha^{\min}, \Pi^{\min}\}$. Thereafter, the result is studied by means of a simple `max`-function applied to $\Pi^{\min}$, which renders $\{\beta^{\text{M opt}}, \beta^{\text{A opt}}\}$ that maximise $\Pi^{\min}$ in states of equilibrium.

Remark 3.1. Note that a closed-form evaluation of the integral in Eq. (29) is generally not available due to the non-linearity of the constitutive model. In analogy to Holzapfel et al. (2000), an $m = 3$-point Gaussian integration scheme with fifth-order accuracy is applied, see Table 4, which turns out to be sufficiently accurate for the computation of the energy expressions and stress contributions of interest within the range of deformations considered.

3.5. *Results*

In the following, the results of the optimisation of the total potential energy functional (29) with respect to different parameters are presented and discussed. The underlying multivariable optimisation problems are performed in view of combinations of five, four, three and two parameters of

Table 4 – Algorithmic determination of functional $\Pi(\lambda_{\theta i}, \lambda_z \doteq \text{const}; \lambda^0_{\theta i}, \boldsymbol{\kappa})$ as given in Eq. (29).

1. Given: material-, structural- and geometrical parameters, see Table 1, and loading parameters, see Table 2, summarised in pseudo-vector $\boldsymbol{\kappa}$
2. Calculate opening angle measure
   $k = 2\pi/[2\pi - \alpha]$
3. Calculate current radii of media
   $r^{\mathrm{M}}_{\mathrm{i}} = \lambda_{\theta i} R^{\mathrm{M}}_{\mathrm{i}}/k$
   $r^{\mathrm{M}}_{\mathrm{o}} = \sqrt{[[R^{\mathrm{M}}_{\mathrm{o}}]^2 - [R^{\mathrm{M}}_{\mathrm{i}}]^2]/[k\lambda_z] + [r^{\mathrm{M}}_{\mathrm{i}}]^2}$
4. Calculate current radii of adventitia
   $r^{\mathrm{A}}_{\mathrm{i}} = r^{\mathrm{M}}_{\mathrm{o}}$
   $r^{\mathrm{A}}_{\mathrm{o}} = \sqrt{[[R^{\mathrm{A}}_{\mathrm{o}}]^2 - [R^{\mathrm{A}}_{\mathrm{i}}]^2]/[k\lambda_z] + [r^{\mathrm{A}}_{\mathrm{i}}]^2}$
5. Apply m=3-point Gaussian quadrature rule for n = M, A with quadrature points $\xi_j = \{-\sqrt{3/5}, 0, \sqrt{3/5}\}$ and weights $w_j = \{5/9, 8/9, 5/9\}$
   loop over number of quadrature points $j = 1, \ldots, m$
   (a) Calculate current radius
   $r_j = [r^{\mathrm{n}}_{\mathrm{i}} + r^{\mathrm{n}}_{\mathrm{o}}]/2 + \xi_j[r^{\mathrm{n}}_{\mathrm{o}} - r^{\mathrm{n}}_{\mathrm{i}}]/2$
   (b) Calculate referential radius
   $R_j = \sqrt{k\lambda_z[r_j^2 - [r^{\mathrm{n}}_{\mathrm{i}}]^2] + [R^{\mathrm{n}}_{\mathrm{i}}]^2}$
   (c) Calculate circumferential stretch
   $\lambda_{\theta j} = k r_j / R_j$
   (d) Calculate strain energy density
   $\Psi^{\mathrm{n}}_j = \tilde{\Psi}^{\mathrm{n}}(\lambda_{\theta j}, \lambda_z \doteq \text{const})$
   by means of Eqs. (50), (51), and (53) calculate internal potential energy
   $\Pi^{\mathrm{n}}_{\mathrm{int}} \approx \pi l[r^{\mathrm{n}}_{\mathrm{o}} - r^{\mathrm{n}}_{\mathrm{i}}] \sum_{j=1}^{m} \Psi^{\mathrm{n}}_j r_j w_j$
6. Calculate external potential energy
   $\Pi_{\mathrm{ext}} = -p\pi[r^{\mathrm{M}}_{\mathrm{i}}]^2 l$
7. Calculate total potential energy
   $\Pi = \Pi^{\mathrm{M}}_{\mathrm{int}} + \Pi^{\mathrm{A}}_{\mathrm{int}} + \Pi_{\mathrm{ext}}$

loading type, $\{\lambda_z, \alpha, p\}$, and structural type, $\{\beta^{\mathrm{n}}\}$, i.e.

$$\min_{\lambda_{\theta i}, \lambda_z, \alpha} \overline{\Pi}(\lambda_{\theta i}, \lambda_z, \alpha; \overline{\boldsymbol{\kappa}}) \tag{66}$$

$$\operatorname*{opt}_{\beta^{\mathrm{M}}, \beta^{\mathrm{A}}; \lambda_{\theta i}, \lambda_z, \alpha} \Pi^{*}(\lambda_{\theta i}, \lambda_z, \alpha, \beta^{\mathrm{M}}, \beta^{\mathrm{A}}; \boldsymbol{\kappa}^{*}) \tag{67}$$

$$\min_{\lambda_{\theta i}, \lambda_z} \tilde{\Pi}(\lambda_{\theta i}, \lambda_z; \tilde{\boldsymbol{\kappa}}) \tag{68}$$

$$\operatorname*{opt}_{\beta^{\mathrm{M}}, \beta^{\mathrm{A}}; \lambda_{\theta i}, \lambda_z} \Pi^{\star}(\lambda_{\theta i}, \lambda_z, \beta^{\mathrm{M}}, \beta^{\mathrm{A}}; \boldsymbol{\kappa}^{\star}) \tag{69}$$

$$\min_{\lambda_{\theta i}, \alpha} \breve{\Pi}(\lambda_{\theta i}, \alpha; \breve{\boldsymbol{\kappa}}) \tag{70}$$

$$\operatorname*{opt}_{\beta^{\mathrm{M}}, \beta^{\mathrm{A}}; \lambda_{\theta i}, \alpha} \Pi^{\diamond}(\lambda_{\theta i}, \alpha, \beta^{\mathrm{M}}, \beta^{\mathrm{A}}; \boldsymbol{\kappa}^{\diamond}) \tag{71}$$

$$\operatorname*{opt}_{\beta; \lambda_{\theta i}} \Pi^{\Delta}(\lambda_{\theta i}, \beta, \beta; \boldsymbol{\kappa}^{\Delta}) \tag{72}$$

Note that $\lambda^0_{\theta i}$ is not explicitly indicated in the energy functions above. Moreover, an identical fibre orientation within the media and adventitia, i.e. $\beta^{\mathrm{M}} = \beta^{\mathrm{A}} = \beta$, is assumed for optimisation problem (72). In order to structure the examples discussed in the following, minimisation problems are typically investigated first, followed by related optimisation studies. Furthermore, the most general cases are addressed first and thereafter reduced to specific applications. In other words, results from the more general cases are transferred to simpler minimisation and optimisation problems in order to render a better illustration of the results obtained.

3.5.1. *Minimisation of* $\overline{\Pi}(\lambda_{\theta i}, \lambda_z, \alpha; \overline{\boldsymbol{\kappa}})$

In the sequel, the minimisation of the three-variable energy functional $\overline{\Pi}$ with respect to the inner circumferential stretch $\lambda_{\theta i}$, the axial (residual) stretch λ_z and the opening angle α is investigated; cf. (66). The pressure is set to the physiological value $p^{\mathrm{phys}} = 13.33$ [kPa].

Fig. 4(a) depicts the solution space $\{\lambda^{\min}_{\theta i}, \lambda_z, \alpha\}$ of the minimisation of $\overline{\Pi}$. The colour code used in Fig. 4(a) illustrates the value of the total potential energy $\Pi^{\min}$; cf. (63). Moreover, Fig. 4(b) shows the total potential energy $\Pi^{\min}$ over λ_z and α, the colour code refers to the primary variable $\lambda^{\min}_{\theta i}$. The red spot at $\lambda^{\min}_{\theta i} = 1.657$, $\lambda^{\min}_{z} = 1.654$ and $\alpha^{\min} = 90.609$ [deg], associated with the solution of the minimisation problem (66), corresponds to the minimal total potential energy $\overline{\Pi}^{\min}$ on this constrained equilibrium-surface, see also Table 5.

Interestingly, the stretch-values $\lambda^{\min}_{\theta i} = 1.657$ and $\lambda^{\min}_{z} = 1.654$ correspond quite well to the physiological values $\lambda^{\mathrm{phys}}_{\theta i} = 1.604$ and $\lambda^{\mathrm{phys}}_{z} = 1.7$. The corresponding opening angle $\alpha^{\min} = 90.609$ [deg], however, differs significantly from its physiological counterpart $\alpha^{\mathrm{phys}} = 160.0$ [deg]. From Fig. 4(a), one observes that in the case of a constant axial stretch λ_z and an increasing opening angle α the inner circumferential stretch $\lambda_{\theta i}$ decreases, whereas the potential energy Π in Fig. 4(b) increases.

3.5.2. *Optimisation of* $\Pi^{*}(\lambda_{\theta i}, \lambda_z, \alpha, \beta^{\mathrm{M}}, \beta^{\mathrm{A}}; \boldsymbol{\kappa}^{*})$

Next, the optimisation of the five-variable energy functional Π^{*} with respect to the inner circumferential stretch $\lambda_{\theta i}$, the axial (residual) stretch λ_z, the opening angle α and both fibre angles β^{M} and β^{A} is discussed; cf. (67). The pressure is set to the physiological value $p^{\mathrm{phys}} = 13.33$ [kPa].

Fig. 5(a) depicts the subset $\{\lambda^{\min}_{\theta i}, \beta^{\mathrm{M}}, \beta^{\mathrm{A}}\}$ of the solution space of the corresponding minimisation of $\overline{\Pi}$. The colour code used in Fig. 5(a) illustrates the value of the minimised total potential energy $\overline{\Pi}^{\min}$; cf. (66). Moreover, Fig. 5(b) shows the total potential energy $\overline{\Pi}^{\min}$ over β^{M} and β^{A}, the colour code refers to the primary variable $\lambda^{\min}_{\theta i}$. The red spot at $\lambda^{\mathrm{opt}}_{\theta i} = 1.676$, $\beta^{\mathrm{M\,opt}} = 29.388$ [deg] and $\beta^{\mathrm{A\,opt}} = 90.000$ [deg], associated with the solution of the optimisation problem (67), corresponds to the optimal total potential energy $\Pi^{*\,\mathrm{opt}}$ on this constrained equilibrium-surface. For ease of reference, essential results are also summarised in Table 6.

Even though the opening angle $\alpha^{\min} = 91.263$ [deg] significantly deviates from the physiological value of $\alpha^{\mathrm{phys}} =$

160.0 [deg], the resulting values for the inner circumferential stretch $\lambda_{\theta i}^{\text{opt}} = 1.676$, the axial (residual) stretch $\lambda_z^{\text{opt}} = 1.593$ and especially the result for the fibre angle in the media $\beta^{\text{M opt}} = 29.388$ [deg] correspond remarkably well to their physiological counterparts $\lambda_{\theta i}^{\text{phys}} = 1.604$, $\lambda_z^{\text{phys}} = 1.7$ and $\beta^{\text{Mphys}} = 29.0$ [deg], see Tables 1 and 2. With regard to the medial fibre angle $\beta^{\text{M opt}}$, the good correspondence may be explained by the fact that the media is by far the stiffest component of an (healthy) artery which consequently carries the main load, especially for the present case of a mean pressure level of $p^{\text{phys}} = 13.33$ [kPa]. In contrast, the influence of the adventitial fibre angle β^{A} on the total potential energy $\overline{\Pi}^{\min}$ for medial fibre angles in the range $\beta^{\text{M}} = 25.0$–50.0 [deg] is almost negligible, i.e. $\overline{\Pi}^{\min} \approx \text{const}$ for $\beta^{\text{A}} \in [0, 90]$ [deg] in the range $\beta^{\text{M}} = 25.0$–50.0 [deg], see Fig. 5(b). This means that – within this range – β^{A} can take any value between 0.0 [deg] and 90.0 [deg] without significant changes in total potential energy $\overline{\Pi}^{\min}$. For larger values of both fibre angles in a range of $\beta^{\text{n}} = 60.0$–90.0 [deg], however, a sudden decrease in total potential energy $\overline{\Pi}^{\min}$ is observed which clearly illustrates the

Table 5 – Results of the minimisation problem (66). The initial values are set to $\lambda_{\theta i}^0 = 1.0$, $\lambda_z^0 = 1.0$ and $\alpha^0 = 90.0$ [deg]. The superscript $\bullet^{\min}$ is omitted.

$\lambda_{\theta i}$ [–]	λ_z [–]	α [deg]	$\overline{\Pi}$ [kPa]
1.657	1.654	90.609	–71.724

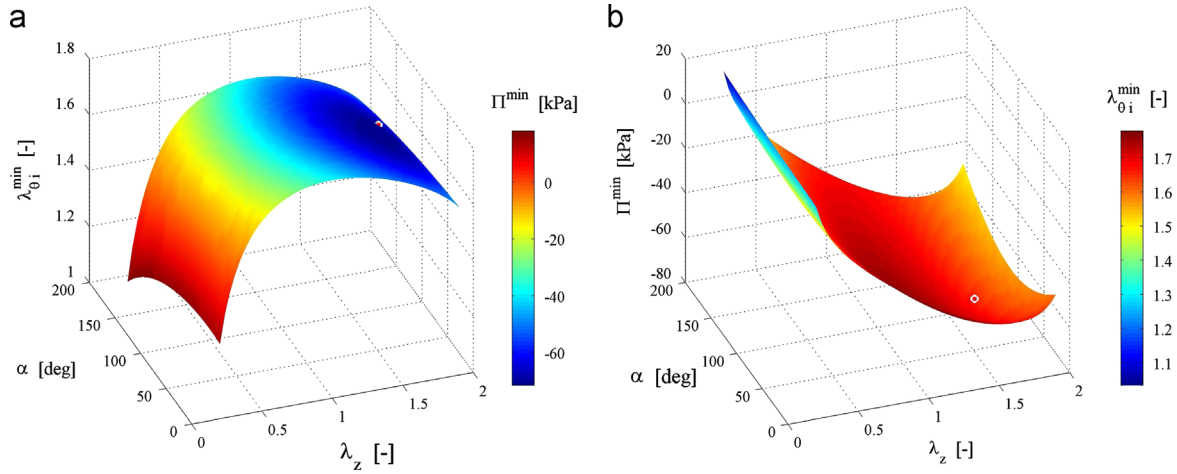

Fig. 4 – Plots of the solution space of minimisation problem (66). (a) Depicts the inner circumferential stretch $\lambda_{\theta i}$ over the axial stretch λ_z and the opening angle α, whereby the colour code refers to the total potential energy $\Pi^{\min}$. (b) Shows the total potential energy $\Pi^{\min}$ over λ_z and α, whereby the colour code refers to the primary variable $\lambda_{\theta i}$. The red spot at $\lambda_{\theta i}^{\min} = 1.657$, $\lambda_z^{\min} = 1.654$ and $\alpha^{\min} = 90.609$ [deg] corresponds to the minimal total potential energy $\overline{\Pi}^{\min}$ on this constrained equilibrium-surface, see also Table 5. (For interpretation of the references to colour in this figure caption, the reader is referred to the web version of this article.)

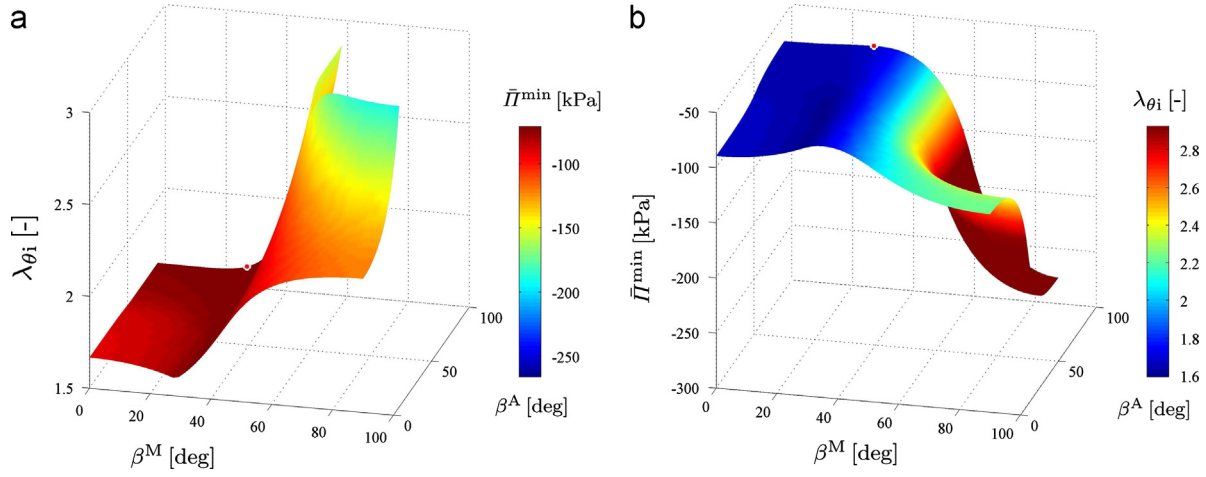

Fig. 5 – Plots of subsets of the solution space of optimisation problem (67). (a) Depicts the inner circumferential stretch $\lambda_{\theta i}^{\min}$ over the medial and adventitial fibre angle β^{M} and β^{A}, whereby the colour code refers to the total potential energy $\overline{\Pi}^{\min}$. (b) Shows the total potential energy $\overline{\Pi}^{\min}$ over β^{M}, β^{A}, whereby the colour code refers to the primary variable $\lambda_{\theta i}^{\min}$. The red spot at $\lambda_{\theta i}^{\text{opt}} = 1.676$, $\beta^{\text{M opt}} = 29.388$ [deg] and $\beta^{\text{A opt}} = 90.000$ [deg] corresponds to the optimal total potential energy $\Pi^{*\text{ opt}}$ on this constrained equilibrium-surface, see also Table 6. (For interpretation of the references to colour in this figure caption, the reader is referred to the web version of this article.)

reduced load bearing capability for fibre angles oriented in almost axial direction of the artery at this particular state of deformation.

Interestingly, fibre angles of $\beta^{M} = 27.551$ [deg] and $\beta^{A} = 34.898$ [deg] lead to a minimal inner circumferential stretch $\lambda_{\theta i} = 1.594$ which obviously is not identical with the location where the optimal total potential energy $\Pi^{*\,opt}$ is obtained. Even if, in this case, the medial fibre angle corresponds quite well to the physiological value again, a significant deviation with respect to the adventitial fibre angle and a large deviation with respect to the inner circumferential stretch is obtained.

3.5.3. *Minimisation of* $\tilde{\Pi}(\lambda_{\theta i}, \lambda_z; \tilde{\boldsymbol{\kappa}})$

The minimisation of the two-variable energy functional $\tilde{\Pi}$ with respect to the inner circumferential stretch $\lambda_{\theta i}$ and the axial (residual) stretch λ_z is discussed as this subsection proceeds; cf. (68). The material, structural and geometrical parameters used are chosen as given in Table 1 and the internal pressure is set to the physiological value of $p^{phys} = 13.33$ [kPa]. Moreover, the opening angle α, associated with the circumferential residual stretch, is assumed as $\alpha^{min} = 90.609$ [deg] which corresponds to the value calculated for the minimisation problem (66), see also Table 5. Practically speaking, the minimisation problem addressed here constitutes a special case of the problem discussed in Section 3.5.1, but allows to conveniently visualise quantities of interest for a pre-fixed value for α.

Fig. 6 shows the (a) internal, (b) external and (c) total potential energy Π over $\lambda_{\theta i}$ and λ_z. Fig. 6(a) and (b) underline the significant influence of the axial stretch λ_z on the internal, as well as on the external potential energy contribution. Using the algorithm summarised in Table 3, the white line within the plot of the total potential energy in Fig. 6(c) is associated with the solution of the minimisation problem (63) and, in consequence, represents the equilibrium-path. The red spot at $\lambda_{\theta i}^{min} = 1.657$ and $\lambda_z^{min} = 1.654$, associated with the solution of the minimisation problem (68), represents the minimum value of the total potential energy on this constrained equilibrium-path; see also the last row in Table 7. It is remarkable that the related value of the (residual) axial stretch value corresponds very well to the assumed physiological value of $\lambda_z^{phys} = 1.7$, cf. also the values in Table 2 which are considered to be physiological.

Moreover, a small parameter study for the minimisation problem (68) is performed by prescribing different combinations of the internal pressure p and the opening angle α. The corresponding results are summarised in Table 7. Within rows 1–4, parameters according to Table 1 are used, whereas row 5 results from the minimisation problem (66) and provides the numerical values of the red spot in Fig. 6. Interestingly, the

Table 6 – Results of the optimisation problem (67). The initial values are set to $\lambda_{\theta i}^{0} = 1.0$, $\lambda_z^{0} = 1.0$, $\alpha^{0} = 90.0$ [deg]. The superscript $\bullet^{opt}$ is omitted.

$\lambda_{\theta i}$ [–]	λ_z [–]	α [deg]	β^{M} [deg]	β^{A} [deg]	Π^{*} [kPa]
1.676	1.593	91.263	29.388	90.000	–70.833

Table 7 – Parameter study of the minimisation problem (68) prescribing different combinations of the internal pressure p and the opening angle α. Within rows 1–4, parameters according to Table 1 are used whereas row 5 results from the minimisation problem (66) and provides the numerical values of the red spot in Fig. 6. The superscript $\bullet^{min}$ is omitted.

Input		output		
p [kPa]	α [deg]	$\lambda_{\theta i}$ [–]	λ_z [–]	$\tilde{\Pi}$ [kPa]
0.000	0.000	1.000	1.000	0.000
13.330	0.000	1.693	1.642	–53.230
0.000	160.000	0.915	1.002	0.015
13.330	160.000	1.616	1.657	–60.600
13.330	90.609	1.657	1.654	–71.720

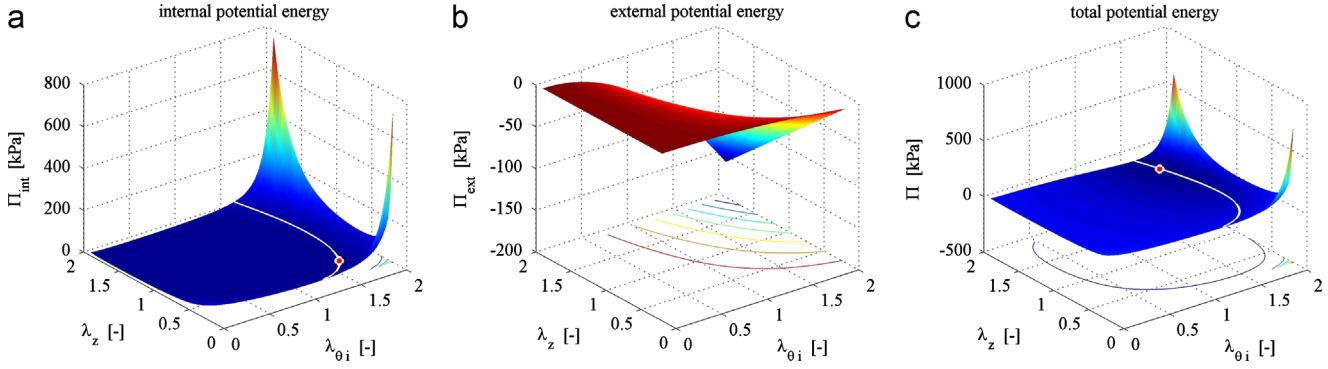

Fig. 6 – Illustration of minimisation problem (68). Surface plot of the (a) internal, (b) external and (c) total potential energy over $\lambda_{\theta i}$ and λ_z for the material, structural and geometrical parameters as given in Table 1 and an internal pressure of $p^{phys} = 13.33$ [kPa]. The opening angle α is assumed as $\alpha^{min} = 90.609$ [deg] as identified by the minimisation problem (66), see Table 5. The white lines in (a) and (c) illustrate the equilibrium-path. The red spot in (a) at $\lambda_{\theta i} = 1.624$ and $\lambda_z = 0.478$ represents the minimal internal potential energy on this constrained equilibrium-path. The red spot in (c) at $\lambda_{\theta i}^{min} = 1.657$ and $\lambda_z^{min} = 1.654$ represents the minimal total potential energy on this constrained equilibrium-path. (For interpretation of the references to colour in this figure caption, the reader is referred to the web version of this article.)

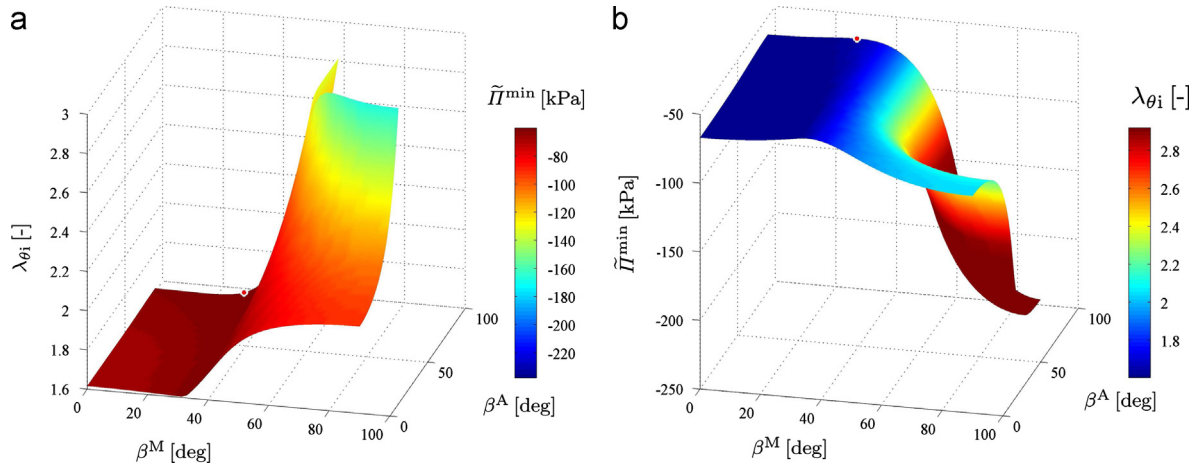

Fig. 7 – Plots of subsets of the solution space of optimisation problem (69). (a) Depicts the inner circumferential stretch $\lambda_{\theta i}^{\min}$ over the medial and adventitial fibre angle β^{M} and β^{A}, whereby the colour code refers to the total potential energy $\tilde{\Pi}^{\min}$. (b) Shows the total potential energy $\tilde{\Pi}^{\min}$ with respect to β^{M}, β^{A}, whereby the colour code refers to the primary variable $\lambda_{\theta i}^{\min}$. The red spot at $\lambda_{\theta i}^{\text{opt}} = 1.638$, $\beta^{M\,\text{opt}} = 29.388$ [deg] and $\beta^{A\,\text{opt}} = 90.000$ [deg] corresponds to the optimal total potential energy $\Pi^{\star\text{opt}}$ on this constrained equilibrium-surface, see also Table 8. (For interpretation of the references to colour in this figure caption, the reader is referred to the web version of this article.)

minimum total potential energy is obtained for $\alpha = 90.609$ [deg], which, however does not yield the minimal inner circumferential stretch $\lambda_{\theta i}$, which is obtained for $\alpha = 160.0$ [deg]. In addition, one observes that the values of the axial stretch λ_z are very similar in the case of $p^{\text{phys}} = 13.33$ [kPa] and correspond very well to the assumed physiological value of $\lambda_z^{\text{phys}} = 1.7$.

3.5.4. *Optimisation of* $\Pi^{\star}(\lambda_{\theta i}, \lambda_z, \beta^{M}, \beta^{A}; \boldsymbol{\kappa}^{\star})$

The optimisation of the four-variable energy functional $\Pi^{\star}$ with respect to the inner circumferential stretch $\lambda_{\theta i}$, the axial (residual) stretch λ_z and both fibre angles β^{M} and β^{A} is addressed in this subsection; cf. (69). The pressure is set to the physiological value $p^{\text{phys}} = 13.33$ [kPa] and the opening angle is fixed as $\alpha^{\text{phys}} = 160.0$ [deg].

Fig. 7(a) depicts the subset $\{\lambda_{\theta i}^{\min}, \beta^{M}, \beta^{A}\}$ of the solution space of the corresponding minimisation of $\tilde{\Pi}$; cf. (68). The colour code illustrates the value of the minimised total potential energy $\tilde{\Pi}^{\min}$. Moreover, Fig. 7(b) shows the total potential energy $\tilde{\Pi}^{\min}$ over β^{M} and β^{A}, the colour code refers to the primary variable $\lambda_{\theta i}^{\min}$. The red spot at $\lambda_{\theta i}^{\text{opt}} = 1.638$, $\beta^{M\,\text{opt}} = 29.388$ [deg] and $\beta^{A\,\text{opt}} = 90.000$ [deg], associated with the solution of the optimisation problem (69), corresponds to the optimal total potential energy $\Pi^{\star\text{opt}}$ on this constrained equilibrium-surface. Essential results are summarised in Table 8. The results obtained, especially with regard to the optimal fibre angles $\beta^{M\,\text{opt}}$ and $\beta^{A\,\text{opt}}$, are qualitatively and quantitatively very similar to the previous ones summarised in Table 6 and illustrated in Fig. 5. In fact the optimisation problem considered in this subsection is a special case of the problem discussed in Section 3.5.2 but with the value of α fixed.

3.5.5. *Minimisation of* $\check{\Pi}(\lambda_{\theta i}, \alpha; \boldsymbol{\kappa})$

The minimisation of the two-variable energy functional $\check{\Pi}$ with respect to the inner circumferential stretch $\lambda_{\theta i}$ and the opening angle α is elaborated on next; cf. (70).

Fig. 8 shows the (a) internal, (b) external and (c) total potential energy $\check{\Pi}$ over $\lambda_{\theta i}$ and α for the parameters as given in Table 1. The axial (residual) stretch is assumed as $\lambda_z^{\min} = 1.654$ and the opening angle, associated with the circumferential residual stretch, is set to $\alpha^{\min} = 90.609$ [deg] as identified by the minimisation problem (66), see also Table 5.

One observes from Fig. 8(a) that the internal potential energy changes slightly with varying opening angle α, while Fig. 8(b) highlights the dependency of the external potential energy on α with minimal values of $\lambda_{\theta i}$ obtained at approximately $\alpha = 100 \pm 10$ [deg]. The white line in the plot of the total potential energy in Fig. 8(c) is associated with the solution of the minimisation problem (63) and, in consequence, represents the equilibrium-path for a prescribed internal pressure of $p^{\text{phys}} = 13.33$ [kPa] and an axial stretch $\lambda_z = 1.654$. The red spot at $\lambda_{\theta i}^{\min} = 1.657$ and $\alpha^{\min} = 90.610$ [deg], associated with the solution of the minimisation problem (70), represents the minimal total potential energy on this constrained equilibrium-path, see also the last row in Table 9.

Moreover, a small parameter study of the minimisation problem (70) is performed by prescribing different combinations of the pressure p and the axial stretch λ_z. The corresponding results are summarised in Table 9. Within rows 1–4, parameters according to Table 1 are used, whereas row 5 results from the minimisation of (66) and gives the numerical values of the red spot in Fig. 8. Interestingly, the minimum total potential energy is obtained for $\lambda_z = 1.654$ which, however, does not yield the minimal inner circumferential stretch $\lambda_{\theta i}$, obtained for $\lambda_z = 1.7$.

3.5.6. *Optimisation of* $\Pi^{\circ}(\lambda_{\theta i}, \alpha, \beta^{M}, \beta^{A}; \boldsymbol{\kappa}^{\circ})$

The optimisation of the four-variable energy functional Π° with respect to the inner circumferential stretch $\lambda_{\theta i}$, the opening angle α and both fibre angles β^{M} and β^{A} is performed next; cf. (71). The pressure is set to the physiological value

$p^{\text{phys}} = 13.33$ [kPa] and the axial (residual) stretch is fixed to $\lambda_z^{\text{phys}} = 1.7$.

Fig. 9(a) depicts the subset $\{\lambda_{\theta i}^{\min}, \beta^{\text{M}}, \beta^{\text{A}}\}$ of the solution space of the corresponding minimisation of Π. The colour code used in Fig. 9(a) illustrates the value of the minimised total potential energy $\check{\Pi}^{\min}$; cf. (70). Moreover, Fig. 9(b) shows the total potential energy $\check{\Pi}^{\min}$ over β^{M} and β^{A}, the colour code refers to the primary variable $\lambda_{\theta i}^{\min}$. The red spot at $\lambda_{\theta i}^{\text{opt}} = 1.832$, $\beta^{\text{M opt}} = 62.449$ [deg] and $\beta^{\text{A opt}} = 90.000$ [deg], associated with the solution of the optimisation problem (71), corresponds to the optimal total potential energy $\Pi^{\circ\,\text{opt}}$ on this constrained equilibrium-surface. Essential results are summarised in Table 10.

Even if it turns out that the resulting values, as summarised in Table 10, are quite different compared to the physiological values, it is worth to note that, in this case, the medial fibre angle of $\beta^{\text{M opt}} = 62.449$ [deg] coincidentally corresponds very well to the assumed physiological adventitial value of $\beta^{\text{A phys}} = 62.0$ [deg]. This enlarged value for the medial fibre angle can be considered as a consequence of the – compared to the previous problems – higher prescribed axial (residual) stretch $\lambda_z = 1.7 = \text{const}$. This results in fibre directions β^{M} closer, but not fully, oriented with respect to the axial direction; see Fig. 10 and the remark below. Similar to the previous observations, however, the adventitial fibre angle seems to be unaffected by these effects and always results in $\beta^{\text{A opt}} = 90.0$ [deg]. Interestingly, fibre angles of $\beta^{\text{M}} = 34.898$ [deg] and $\beta^{\text{A}} = 53.265$ [deg] lead to a minimal inner circumferential stretch $\lambda_{\theta i} = 1.643$ which again is not identical with the state at which the minimal total potential energy is obtained.

In addition to the results displayed in Fig. 9, the relation between the axial stretch λ_z, internal pressure p and medial fibre angle $\beta^{\text{M opt}}$ is illustrated in Fig. 10, where the colour code refers to the optimal fibre angle $\beta^{\text{M opt}}$ corresponding to a particular loading state defined by λ_z and p. The opening angle is assumed as $\alpha^{\text{phys}} = 160.0$ [deg]. The physiological region corresponding to $p^{\text{phys}} = 8.0$–17.4 [kPa] and $\lambda_z^{\text{phys}} = 1.65$–$1.75$ is marked by a white-shaded rectangle.

It is obvious from Fig. 10 that for low axial stretch values but high pressure, favourable fibre angles are oriented towards the circumferential direction, i.e. $\beta^{\text{M opt}} = 0.0$ [deg], which is indicated by the dark blue colour in the upper left region. In contrast, a fibre angle aligned with respect to the axial direction, i.e. $\beta^{\text{M opt}} = 90.0$ [deg], is obtained for high values of the axial stretch but low pressure as indicated by the dark red colour in the lower right. However, for high axial stretch values of $\lambda_z = 1.8$–1.9, irrespective of the pressure magnitude, one permanently obtains a fibre angle aligned with respect to the axial direction. Interestingly, there is a

Table 8 – Results of the minimisation problem (69). The initial values are set to $\lambda_{\theta i}^0 = 1.0$ and $\lambda_z^0 = 1.0$. The superscript $\bullet^{\text{opt}}$ is omitted.

$\lambda_{\theta i}$ [–]	λ_z [–]	β^{M} [deg]	β^{A} [deg]	$\Pi^{\star}$ [kPa]
1.638	1.587	29.388	90.000	–60.053

Table 9 – Parameter study of the minimisation problem (70) prescribing different combinations of the pressure p and the axial stretch λ_z. Within rows 1–4, parameters according to Table 1 are used, whereas row 5 results from the minimisation problem (66) and provides the numerical values of the red spot in Fig. 8. The superscript $\bullet^{\min}$ is omitted.

Input		Output		
p [kPa]	λ_z [–]	$\lambda_{\theta i}$ [–]	α [deg]	$\check{\Pi}$ [kPa]
0.000	1.000	1.000	–0.001	0.000
13.330	1.000	1.743	90.040	–50.920
0.000	1.700	–	–	—
13.330	1.700	1.644	90.460	–71.510
13.330	1.654	1.657	90.610	–71.720

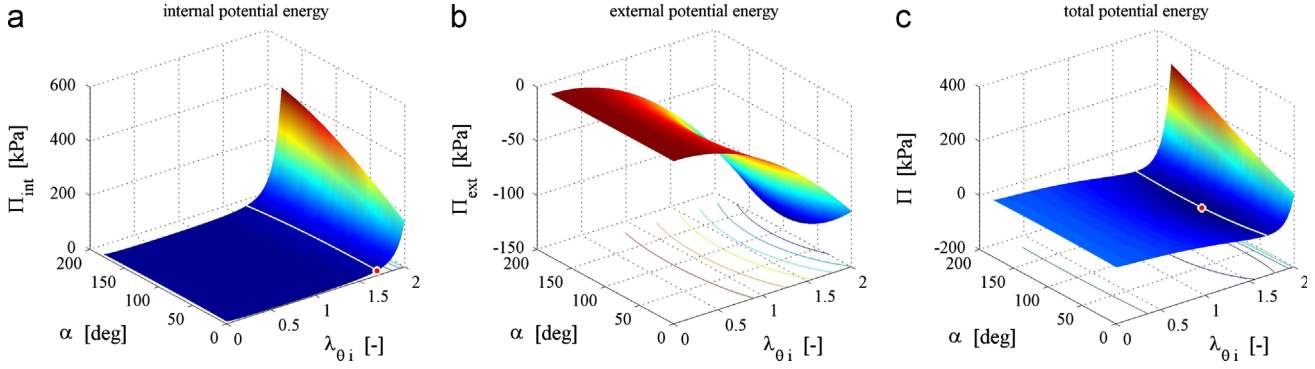

Fig. 8 – Illustration of minimisation problem (70). Surface plot of the (a) internal, (b) external and (c) total potential energy over $\lambda_{\theta i}$ and α for the parameters as given in Table 1. The axial residual stretch λ_z is assumed as $\lambda_z^{\min} = 1.654$ and the opening angle α, associated with the circumferential residual stretch, is set to $\alpha^{\min} = 90.609$ [deg] as identified by the minimisation problem (67), see also Table 5. The white lines in (a) and (c) illustrate the equilibrium-path. The red spot in (a) at $\lambda_{\theta i} = 1.6895$ and $\alpha = 0.0$ [deg] represents the minimal internal potential energy on this constrained equilibrium-path. The red spot at $\lambda_{\theta i}^{\min} = 1.657$ and $\alpha^{\min} = 90.610$ [deg] represents the minimal total potential energy on this constrained equilibrium-path. (For interpretation of the references to colour in this figure caption, the reader is referred to the web version of this article.)

physiologically characteristic region indicated in yellow, where the fibre angle and the axial stretch remain almost constant, i.e. $\beta^{M\,opt} \approx 62.0$ [deg] and $\lambda_z \approx 1.7$, respectively. For pressures being located within the physiological range, i.e. $p = 8.0$–17.4 [kPa], one consequently observes only slight variations with respect to the axial stretch, i.e. $\lambda_z \approx 1.7$ for a fibre angle of $\beta^{M\,opt} \approx 62.0$ [deg], which illustratively underlines the physiological suitability of these values.

3.5.7. *Optimisation of $\Pi^{\triangle}(\lambda_{\theta i}, \beta, \beta; \kappa^{\triangle})$*

The optimisation of the two-variable energy functional Π° with respect to the inner circumferential stretch $\lambda_{\theta i}$ and the fibre angle β is focussed on in this section, cf. (72).

Fig. 11 shows the (a) internal, (b) external and (c) total potential energy with respect to $\lambda_{\theta i}$ and β for the parameters as given in Table 1. The fibre angles β^M and β^A are assumed to be identical for both layers, i.e. $\beta = \beta^M = \beta^A$. The axial residual stretch λ_z is assumed as $\lambda_z^{min} = 1.654$ and the opening angle α, associated with the circumferential residual stretch, is set to $\alpha^{min} = 90.609$ [deg] as identified by the minimisation problem (66), see also Table 5. One observes from Fig. 11(a) that the internal potential energy landscape varies significantly with the fibre angle β while Fig. 11(b) shows, as expected, the external potential energy to be constant in β. The white line in the plot of the total potential energy in Fig. 11(c) is associated with the solution of the minimisation problem (63) and consequently represents the equilibrium-path for a prescribed internal pressure of $p^{phys} = 13.33$ [kPa], an axial stretch of $\lambda_z = 1.654$ and an opening angle of $\alpha = 90.609$ [deg]. The red spot at $\lambda_{\theta i}^{opt} = 1.765$ and $\beta^{opt} = 53.265$ [deg], associated with the solution of the optimisation problem (72), represents an extremum of the total potential energy on this constrained equilibrium-path; see also the last row in Table 11.

Moreover, a small parameter study of the optimisation problem (72) is performed prescribing different combinations of the pressure p, the axial stretch λ_z and the opening angle α. The corresponding results are summarised in Table 11. Within rows 1–8, parameters according to Table 1 are used, whereas row 9 results from the minimisation problem (66)

Table 10 – Results of the optimisation problem (71). The initial values are set to $\lambda_{\theta i}^0 = 1.0$ and $\alpha^0 = 90.0$ [deg]. The superscript $\bullet^{opt}$ is omitted.

$\lambda_{\theta i}$ [–]	α [deg]	β^M [deg]	β^A [deg]	Π° [kPa]
1.832	89.861	62.449	90.000	–50.298

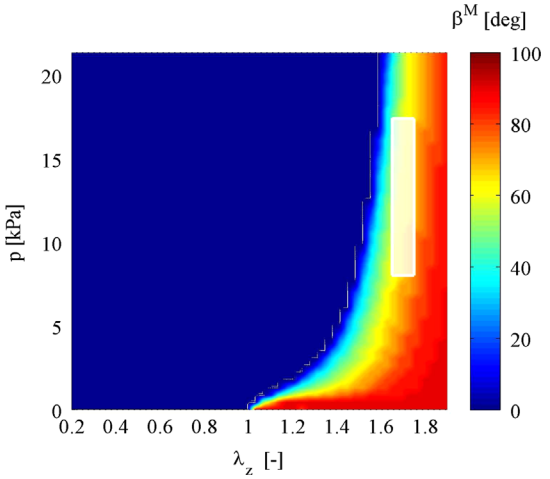

Fig. 10 – Illustration of the relation between the axial stretch λ_z, internal pressure p and (optimal) fibre angle $\beta^{M\,opt}$ as indicated by the colour code. The opening angle is assumed as $\alpha^{phys} = 160.0$ [deg]. The white rectangle is associated with the physiological region corresponding to $p^{phys} = 8.0$–17.4 [kPa] and $\lambda_z^{phys} = 1.65$–1.75. (For interpretation of the references to colour in this figure caption, the reader is referred to the web version of this article.)

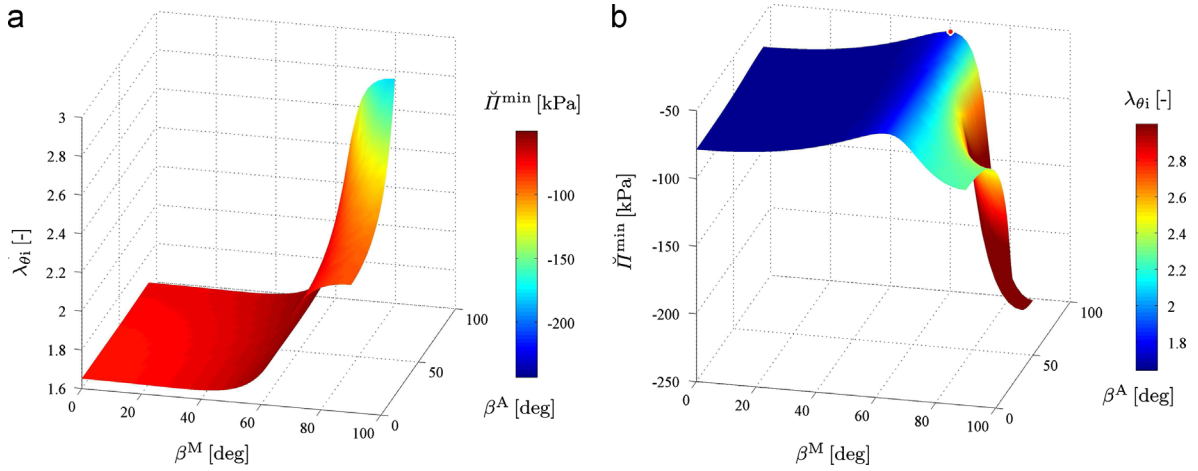

Fig. 9 – Plots of subsets of the solution space of optimisation problem (71). (a) Depicts the inner circumferential stretch $\lambda_{\theta i}^{min}$ over the medial and adventitial fibre angle β^M and β^A, whereby the colour code refers to the total potential energy Π. (b) Shows the total potential energy Π with respect to β^M and β^A, whereby the colour code refers to the primary variable $\lambda_{\theta i}^{min}$. The red spot at $\lambda_{\theta i}^{opt} = 1.8323$, $\beta^{M\,opt} = 62.449$ [deg] and $\beta^{A\,opt} = 90.000$ [deg] corresponds to the optimal total potential energy $\Pi^{\circ\,opt}$ on this constrained equilibrium-surface, see also Table 10. (For interpretation of the references to colour in this figure caption, the reader is referred to the web version of this article.)

and provides the numerical values of the red spot in Fig. 11. It becomes apparent that the incorporation of a circumferential residual stress by means of an opening angle $\alpha > 0.0$ tends to reduce the obtained circumferential stretch $\lambda_{\theta i}$. As expected, one obtains a fibre angles of $\beta = 0.0$ [deg] for parameter combinations including $p \neq 0.0$ [kPa] and $\lambda_z = 1.0$. Similarly, a fibre angle of $\beta = 90.0$ [deg] is observed for a parameter combination considered with $p = 0.0$ [kPa] and $\lambda_z \neq 1.0$. Furthermore, the minimum total potential energy is obtained for $\lambda_z = 1.654$ and $\alpha = 90.609$ [deg] which, however, does not yield the minimal inner circumferential stretch $\lambda_{\theta i}$ for the parameter settings considered—the related minimal values are $\lambda_z = 1.0$ and $\alpha = 160.0$ [deg].

Based on optimisation problem (72), the interaction between the pressure p, the opening angle α, the fibre angle β and the axial stretch λ_z is investigated. A physiological value of the axial (residual) stretch of $\lambda_z^{\text{phys}} = 1.7$ is used according to Holzapfel et al. (2000). Under the action of real blood flow, i.e. changing values of internal pressure p, it is obvious that the axial elongation of an artery should not vary significantly. In other words, a change of λ_z for different values of p should not significantly influence other quantities of interest such as the inner circumferential stretch $\lambda_{\theta i}$. In this context, the primal aim is to find out whether parameter sets exist with regard to p, α and especially β, which render the optimal axial stretch to be almost unchanged, i.e. $\lambda_z = \text{const}$.

Fig. 12 shows the axial stretch λ_z over the inner circumferential stretch $\lambda_{\theta i}$ and the fibre angle β for different pressures of $p = \{8.0, 13.3, 17.4\}$ [kPa] (from top to bottom) and for different opening angles $\alpha = \{0.0, 80.0, 160.0\}$ [deg] (from left to right). With regard to the constant axial stretch range of about $\lambda_z = 0.0$–1.7, one observes that the inner circumferential stretch $\lambda_{\theta i}$ increases with increasing values of the fibre angle β. It is of interest to note that this effect is reversed for approximately $\lambda_z > 1.7$. In other words, $\lambda_{\theta i}$ first may decrease with β but for larger values of β significantly increases with β, which clearly is a consequence of the pronounced material properties in these directions. Moreover, one observes that a plateau-type characteristic exists for $\beta = 60.0$–80.0 [deg], where the axial stretch remains almost unchanged within the range $\lambda_z \in [1.7, 1.8]$. Furthermore, even if not clearly illustrated in Fig. 12, the values of the inner circumferential stretch $\lambda_{\theta i}$ increase with increasing internal pressure p. Practically speaking, the entire surface is shifted towards larger values of $\lambda_{\theta i}$. An increase of the opening angle α, however, causes the inner circumferential stretch $\lambda_{\theta i}$ to decrease, i.e. the entire surface is shifted towards smaller values of $\lambda_{\theta i}$.

Fig. 13 illustrates the inner circumferential stretch $\lambda_{\theta i}$ over the fibre angle $\beta = \beta^{\text{M}} = \beta^{\text{A}}$ for different pressures $p = \{8.0, 13.3, 17.4\}$ [kPa] and different axial (residual) stretches $\lambda_z = \{1.6, 1.65, 1.7, 1.75\}$. The opening angle is set to $\alpha = 160.0$ [deg] which corresponds to the red curves in the right column of Fig. 12. One observes from Fig. 13(a) and (b), which respectively refer to axial stretches of $\lambda_z = 1.6$ and $\lambda_z = 1.65$, that $\lambda_{\theta i}$ increases with increasing fibre angles β (except the curve for $p = 8.0$ [kPa]). This behaviour, however, significantly changes for the graphs in Fig. 13(c) and (d), i.e. for axial

Table 11 – Parameter study of the optimisation problem (72) prescribing different combinations of the pressure p, the axial stretch λ_z and the opening angle α. Within rows 1–8, parameters according to Table 1 are used, whereas row 9 results from the minimisation problem (66) and provides the numerical values of the red spot in Fig. 11. The superscript $\bullet^{\text{opt}}$ is omitted.

Input			Output		
p [kPa]	λ_z [–]	α [deg]	$\lambda_{\theta i}$[–]	β [deg]	Π^* [kPa]
13.330	1.000	0.000	1.594	0.000	–31.074
0.000	1.700	0.000	0.767	90.000	59.448
13.330	1.700	0.000	1.896	64.286	–34.256
13.330	1.000	160.000	1.510	0.000	–34.329
13.330	1.700	160.000	1.798	64.286	–40.034
13.330	1.654	90.609	1.765	53.265	–66.907

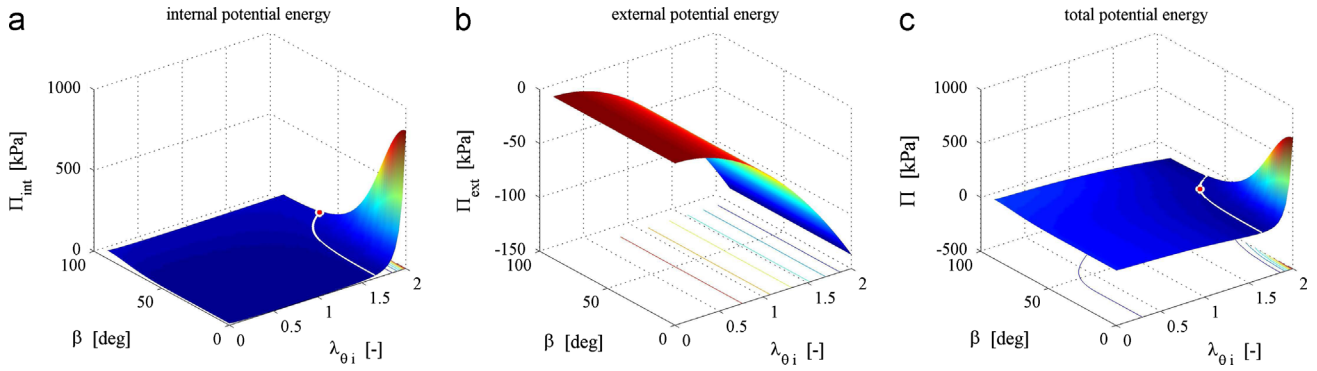

Fig. 11 – Illustration of optimisation problem (72). Surface plot of the (a) internal, (b) external and (c) total potential energy Π over $\lambda_{\theta i}$ and β for the parameters as given in Table 1 with $\beta = \beta^{\text{M}} = \beta^{\text{A}}$. The axial residual stretch λ_z is assumed as $\lambda_z^{\min} = 1.654$ and the opening angle α, associated with the circumferential residual stretch, is set to $\alpha^{\min} = 90.609$ [deg] as identified by the minimisation problem (66), see also Table 5. The white lines in (a) and (c) illustrate the equilibrium-path. The red spot in (a) at $\lambda_{\theta i} = 1.9797$ and $\beta = 62.449$ [deg] represents the minimal internal potential energy on this constrained equilibrium-path. The red spot in (c) at $\lambda_{\theta i}^{\text{opt}} = 1.765$ and $\beta^{\text{opt}} = 53.265$ [deg] represents the minimal total potential energy on this constrained equilibrium-path. (For interpretation of the references to colour in this figure caption, the reader is referred to the web version of this article.)

stretches of $\lambda_z = 1.7$ and $\lambda_z = 1.75$. In theses cases, $\lambda_{\theta i}$ first decreases with increasing fibre angles β until a minimum value is obtained and then increases with β. It is interesting to note that for the largest axial stretch considered, here $\lambda_z = 1.75$, the smallest inner circumferential stretches are obtained. These minimum values, for the respective pressure values chosen, also refer to different fibre angles β as for smaller axial stretches. Moreover, one observes that in (c) almost constant values for $\lambda_{\theta i}$ are obtained for $\beta = 0$–40 [deg], whereas β turns out to remain almost constant for $\lambda_{\theta i} > 1.8$. The spots in the graphs of Fig. 13(a)–(d) refer to the optimisation problem (72). One observes especially from Fig. 13(c) and (d) that the minimal circumferential stretch values and the values resulting in a minimal total potential energy are not identical.

In addition to the previous plots, Fig. 14 shows – by way of illustration and comparison – the distributions of the Cauchy stresses over the width of the deformed tube. Three different cases of residual stress states are considered as represented by the opening angles $\alpha = \{0.0, 90.601, 160.0\}$ [deg] in combination with a physiological pressure of $p^{\text{phys}} = 13.33$ [kPa] and an axial (residual) stretch of $\lambda_z = 1.0$. The opening angle of $\alpha = 90.601$ [deg] corresponds to the solution of the minimisation problem (66), see also Table 5. Fig. 14(a) shows that the radial stress σ_{rr} – in contrast to the tangential stresses $\sigma_{\theta\theta}$ and σ_{zz} – turns out to be continuous over the width of the tube, which is a consequence of the contribution of the equilibrium condition in radial direction, see Eq. (45). Note, that the boundary conditions $\sigma_{rr}|_{r_i^M} = -13.33$ [kPa] at the inner boundary and $\sigma_{rr}|_{r_o^A} = 0.0$ [kPa] at the outer boundary are met. Moreover, the circumferential stress $\sigma_{\theta\theta}$ constitutes the dominant stress coefficient within the wall of the tube, since its magnitude is significantly larger compared to the magnitudes of σ_{rr} and σ_{zz}. In case residual stresses are accounted for via the opening angle α, the circumferential and axial stresses $\sigma_{\theta\theta}$ and σ_{zz} obviously decrease at the inner wall but increase at the outer wall, as can be seen in Fig. 14(b) and (c). Practically speaking, the gradient of $\sigma_{\theta\theta}$ and σ_{zz} with respect to r in the media is reduced so that their distributions are more, say, homogenised. As an interesting side aspect, the mean stresses of $\sigma_{\theta\theta}$ and σ_{zz} through the wall-thickness increase in case residual stresses are included, although residual stress reduces the maximal circumferential and axial stresses at the inner wall significantly. In contrast to this, the radial stress coefficient σ_{rr} increases from the inner boundary of the wall to its outer boundary and, moreover, the related graphs possess a kink at the interface between the media and adventitia due to the change of material parameters.

4. Summary

Various biological tissues are designed to optimally support external mechanical loads within complex geometries and mechanobiological structures. This may result in complex microstructures of these materials. In this work, emphasis is placed on the modelling and simulation of arteries. The arterial wall can be considered as a multi-layered composite,

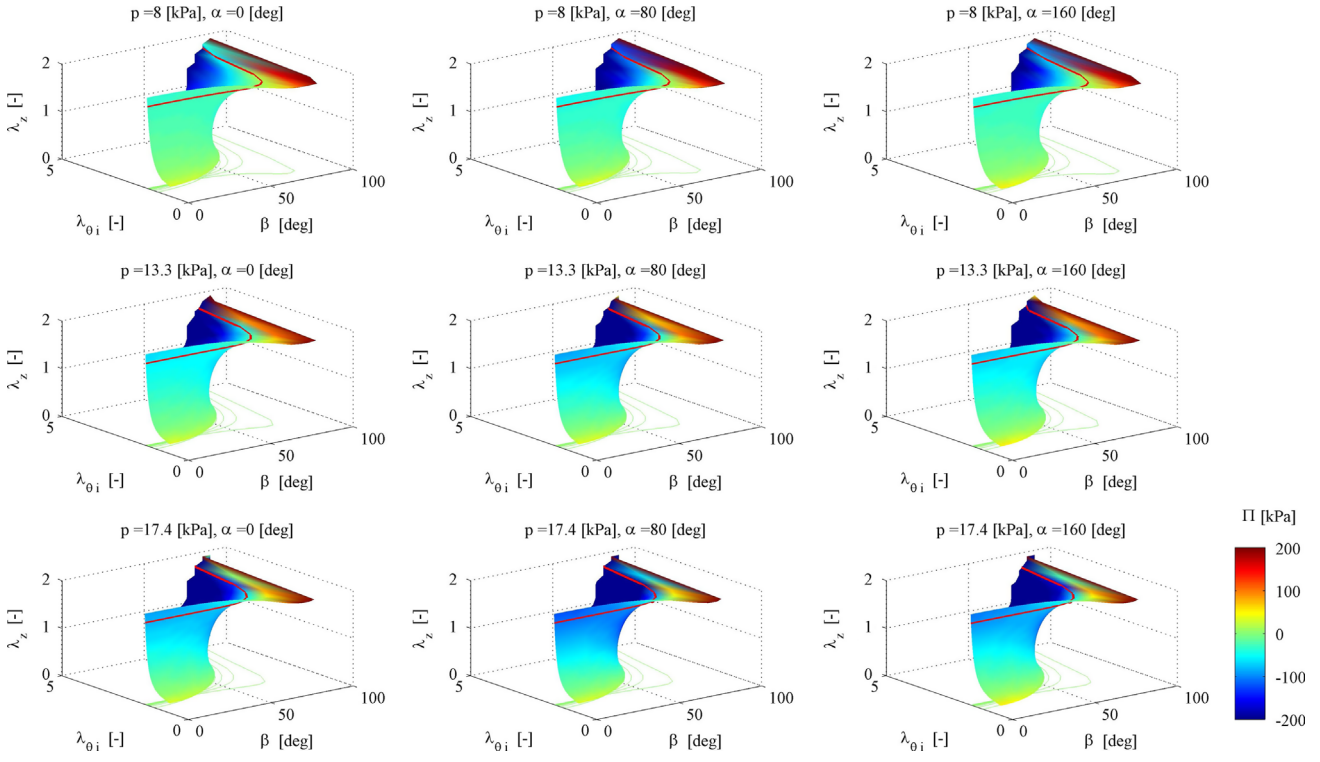

Fig. 12 – Axial stretch λ_z plotted over the inner circumferential stretch $\lambda_{\theta i}$ and the fibre angle β for different pressures $p = \{8.0, 13.3, 17.4\}$ [kPa] (from top to bottom) and different opening angles $\alpha = \{0.0, 80.0, 160.0\}$ [deg] (from left to right). The colour code illustrates the total potential energy Π and the red line represents an exemplary isoline for $\lambda_z = \text{const}$ to be further studied in Fig. 13. (For interpretation of the references to colour in this figure caption, the reader is referred to the web version of this article.)

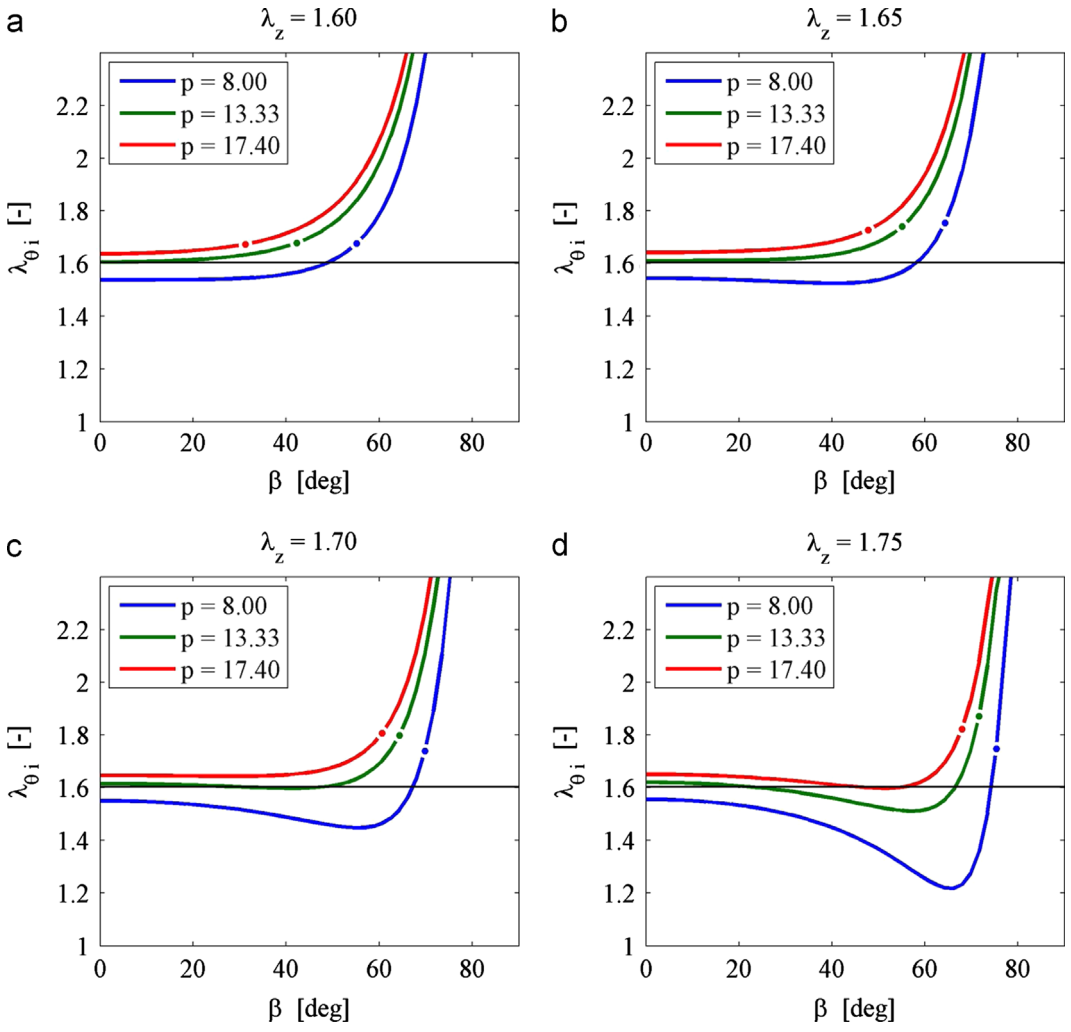

Fig. 13 – Inner circumferential stretch $\lambda_{\theta i}$ plotted over the fibre angle $\beta = \beta^{M} = \beta^{A}$ for different pressures $p = \{8.0, 13.3, 17.4\}$ [kPa] and different axial (residual) stretches $\lambda_z = \{1.6, 1.65, 1.7, 1.75\}$ and an opening angle of $\alpha = 160.0$ [deg] corresponding to the red line in the right column of Fig. 12. The horizontal black line indicates the physiological value of the circumferential stretch $\lambda_{\theta i}^{phys} = 1.604$ which, according to Table 2 corresponds to $\lambda_z^{phys} = 1.7$, $p^{phys} = 13.33$ [kPa] and $\alpha^{phys} = 160.0$ [deg]. The spots indicate the values obtained form the optimisation problem (72).

whereby the respective layers possess anisotropic material properties due to, e.g. the distribution of collagen fibres. As a prototype example, typically a double-layered thick-walled cylindrical tube subjected to internal blood pressure is assumed to represent a healthy in vivo artery. As a key aspect of the model, states of residual stresses are incorporated which significantly influence the overall mechanical properties of the artery.

A main focus of this work is to investigate the interaction between the mechanical loading levels of the artery, its residual stress states and material, respectively structural, properties such as representative fibre orientations. Motivated by the postulate of the stationary of the total potential energy, a key contribution of the present work is to access additional information on preferred material, structural and loading parameters by direct minimisation of the total potential energy with respect to the parameters of interest in the context of the particular boundary value problem at hand. From the energetic point of view, these quantities calculated are considered to be favourable for the design and adaptation of arterial walls.

An established constitutive model together with a framework to include states of residual stresses is adopted as the development of a new material model is not in the focus of the present work. In fact, the energy-based framework discussed can be transferred to any suitable continuum-mechanics-based constitutive model. Alternative approaches, not addressed in this work may be referred to, e.g. a homogeneous target stress distribution. The overall level of the total potential energy is strongly influenced by the material and structural properties and the residual stresses state. The results obtained for the analysis performed in this work can directly be referred to turnover and remodelling phenomena which are related to reorientation processes of the respective fibre families induced by, e.g. mechanical stimuli. To give an example, the deployment of a stent changes the state of loading in an artery so that a change in fibre orientation may result in an energetically favourable

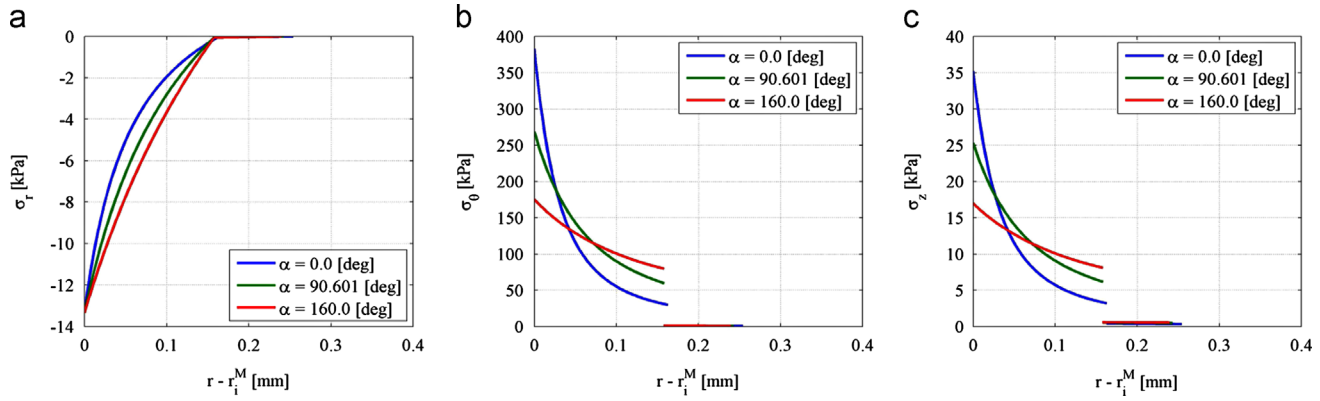

Fig. 14 – Plots of the principal Cauchy stresses $\sigma_{rr,\theta\theta,zz}$ over the width $r-r_i^M$ of the deformed tube for three different opening angles $\alpha = \{0.0, 90.601, 160.0\}$ [deg] together with $p = 13.33$ [kPa] and $\lambda_z = 1.0$: (a) radial stress σ_{rr}, (b) circumferential stress $\sigma_{\theta\theta}$, and (c) axial stress σ_{zz}.

state. This can be considered as a criterion for a computational remodelling framework.

Several numerical examples given in this work show that the values calculated for, e.g. the axial residual stretch, the opening angle or the fibre angles are in good agreement with physiological values reported in the literature. In this regard, a physiologically important property of arteries is their ability to (almost) maintain their length under the action of blood flow. In other words, the length or rather axial stretch within the artery remains (almost) constant under blood pressure loading within the physiologically relevant limits. The investigation of extremal states of total potential energy allows us to identify combinations of residual stresses – including a residual stretch in axial direction – and fibre orientation angles which render the total potential energy to remain (almost) constant within the interval of physiological blood pressures. This illustratively underlines the physiological suitability of the identified values and motivates to transfer the framework established in this work to other loading scenarios, such as stent deployment or the deposition of plaques with age-dependent properties. The energetically favourable states of residual stress and fibre orientations for these modified cases can motivate related computational models for turn-over and remodelling phenomena.

In addition to the modelling of time-dependant turn-over and remodelling processes, future research shall include complex geometries in combination with advanced finite element formulations. From the computational modelling point of view, this naturally extends the almost analytical investigations of this work towards the simulation of patient-specific mechanobiological structures. Moreover, the combination of the constitutive model with inelastic effects, such as damage phenomena and active stress contributions, constitute an attractive line of future research work.

REFERENCES

Alastrué, V., Martínez, M., Doblaré, M., Menzel, A., 2009. Anisotropic micro-sphere-based finite elasticity applied to blood vessel modelling. Journal of the Mechanics and Physics of Solids 57, 178–203.

Alastrué, V., Peña, E., Martínez, M., Doblaré, M., 2007. Assessing the use of the "Opening Angle Method" to enforce residual stresses in patient-specific arteries. Annals of Biomedical Engineering 35, 1821–1837.

Alford, P., Humphrey, J., Taber, L., 2008. Growth and remodeling in a thick-walled artery model: effects of spatial variations in wall constituents. Biomechanics and Modeling in Mechanobiology 7, 245–262.

Ambrosi, D., Ateshian, G., Arruda, E., Cowin, S., Dumais, J., Goriely, A., Holzapfel, G., Humphrey, J., Kemkemer, R., Kuhl, E., Olberding, J., Taber, L., Garikipati, K., 2011. Perspectives on biological growth and remodeling. Journal of the Mechanics and Physics of Solids 59, 863–883.

Balzani, D., Böse, D., Brands, D., Erbel, R., Klawonn, A., Rheinbach, O., Schröder, J., 2012. Parallel simulation of patient-specific atherosclerotic arteries for the enhancement of intravascular ultrasound diagnostics. Engineering Computations 29, 888–906.

Bertsekas, D., 1996. Constrained optimization and Lagrange multiplier methods. Athena Scientific Optimization and Computation Series, vol. 4. Athena Scientific.

Boehler, J. (Ed.), 1987. Applications of Tensor Functions in Solid Mechanics. CISM Courses and Lectures, vol. 292. Springer, Wien, New York.

Bonet, J., Wood, R., 1997. Nonlinear Continuum Mechanics for Finite Element Analysis. Cambridge University Press.

Cardamone, L., Valentín, A., Eberth, J., Humphrey, J., 2009. Origin of axial prestretch and residual stress in arteries. Biomechanics and Modeling in Mechanobiology 8, 431–446.

Chuong, C., Fung, Y., 1983. Three-dimensional stress distribution in arteries. Journal of Biomechanical Engineering 105, 268–274.

Creane, A., Kelly, D.J., Lally, C., 2012. Patient specific computational modeling in cardiovascular mechanics. In: Calvo Lopez, B., Peña, E. (Eds.), Patient-Specific Computational Modeling. Springer Netherlands. Lecture Notes in Computational Vision and Biomechanics, vol. 5. pp. 61–79.

Dennis Jr., J., Schnabel, R., 1996. Numerical Methods for Unconstrained Optimization and Nonlinear Equations. Classics in Applied Mathematics, vol. 16. SIAM, Society for Industrial and Applied Mathematics, Philadelphia.

Driessen, N.J.B., Wilson, W., Bouten, C.V.C., Baaijens, F.P.T., 2004. A computational model for collagen fibre remodelling in the arterial wall. Journal of Theoretical Biology 226, 53–64.

Gasser, T., Ogden, R., Holzapfel, G., 2006. Hyperelastic modelling of arterial layers with distributed collagen fibre orientations. Journal of the Royal Society Interface 3, 15–35.
Gent, A., Rivlin, R., 1952. Experiments on the mechanics of rubber II: the tension, inflation and extension of a tube. Proceedings of the Physical Society B 65, 487–501.
Green, A., Adkins, J., 1970. Large Elastic Deformations, 2nd edition Oxford University Press.
Haughton, D., 2001. Elastic membranes. In: Fu, Y., Ogden, R. (Eds.), Nonlinear Elasticity: Theory and Applications. London Mathematical Society Lecture Notes Series, vol. 283, Cambridge, pp. 97–134.
Haughton, D., Ogden, R., 1979. Bifurcation of inflated circular cylinders of elastic material under axial loading-I. Membrane theory for thin-walled tubes. Journal of the Mechanics and Physics of Solids 27, 179–212.
Haughton, D., Ogden, R., 1980a. Bifurcation of rotating thick-walled elastic tubes. Journal of the Mechanics and Physics of Solids 28, 59–74.
Haughton, D.M., Ogden, R.W., 1980b. Bifurcation of finitely deformed rotating elastic cylinders. Quarterly Journal of Mechanics and Applied Mathematics 33, 251–266.
Hoger, A., 1985. On the residual stress possible in an elastic body with material symmetry. Archive for Rational Mechanics and Analysis 88, 271–290.
Hoger, A., 1986. On the determination of residual stress in an elastic body. Journal of Elasticity 16, 303–324.
Hoger, A., 1993. The dependence of the elasticity tensor on residual stress. Journal of Elasticity 33, 145–165.
Holzapfel, G., Gasser, T., Ogden, R., 2000. A new constitutive framework for arterial wall mechanics and a comparative study of material models. Journal of Elasticity 61, 1–48.
Holzapfel, G., Ogden, R. (Eds.), 2003. Biomechanics of Soft Tissue in Cardiovascular Systems. CISM Courses and Lectures, vol. 441. Springer, Wien, New York.
Holzapfel, G., Ogden, R. (Eds.), 2009. Biomechanical Modelling at the Molecular, Cellular and Tissue Levels. CISM Courses and Lectures, vol. 508. Springer, Wien, New York.
Holzapfel, G., Ogden, R., 2010. Constitutive modelling of arteries. Proceedings of the Royal Society A. Mathematical, Physical and Engineering Sciences 466, 1551–1597.
Humphrey, J., 2002. Cardiovascular Solid Mechanics. Cells, Tissues, and Organs. Springer.
Humphrey, J., Rajagopal, K., 2002. A constrained mixture model for growth and remodeling of soft tissues. Mathematical Models and Methods in Applied Sciences 12, 407–430.
Johnson, B., Hoger, A., 1995. The use of virtual configuration in formulating constitutive equations for residually stressed elastic materials. Journal of Elasticity 41, 177–215.
Luenberger, D., 1984. Nonlinear Programming, 2nd edition Addison-Wesley, Reading, Massachusetts.
Malvern, L., 1969. Introduction to the Mechanics of a Continuous Medium. Prentice-Hall.
Menzel, A., 2005. Modelling of anisotropic growth in biological tissues – a new approach and computational aspects. Biomechanics and Modeling in Mechanobiology 3, 147–171.
Menzel, A., 2007. A fibre reorientation model for orthotropic multiplicative growth – configurational driving stresses, kinematics-based reorientation, and algorithmic aspects. Biomechanics and Modeling in Mechanobiology 6, 303–320.
Menzel, A., Harrysson, M., Ristinmaa, M., 2008. Towards an orientation-distribution-based multi-scale approach for remodelling biological tissues. Computer Methods in Biomechanics and Biomedical Engineering 11, 505–524.
Menzel, A., Kuhl, E., 2012. Frontiers in growth and remodeling. Mechanics Research Communications 42, 1–14.
Menzel, A., Waffenschmidt, T., 2009. A micro-sphere-based remodelling formulation for anisotropic biological tissues. Philosophical Transactions of the Royal Society A 367, 3499–3523.
Noll, W., 1967. Materially uniform simple bodies with inhomogeneities. Archive for Rational Mechanics and Analysis 27, 1–32 Errata: W. Noll, R.A. Toupin, C.C. Wang. Archive for Rational Mechanics and Analysis, 31(5):401, 1968.
Ogden, R., 1997. Non-Linear Elastic Deformations. Dover.
Ogden, R., 2001. Elements of the theory of finite elasticity. In: Fu, Y., Ogden, R. (Eds.), Nonlinear Elasticity: Theory and Applications. London Mathematical Society Lecture Notes Series, vol, 283, Cambridge, pp. 97–134.
Olsson, T., Stålhand, J., Klarbring, A., 2006. Modeling initial strain distribution in soft tissues with application to arteries. Biomechanics and Modeling in Mechanobiology 5, 27–38.
Pipkin, A., Rivlin, R., 1962. Minimum-weight design for pressure vessels reinforced with inextensible fibres. ASME Journal of Applied Mechanics WA-151.
Podio-Guidugli, P., Vergara Caffarelli, G., 1990. Surface interaction potentials in elasticity. Archive for Rational Mechanics and Analysis 109, 343–383.
Rissland, P., Alemu, Y., Einav, S., Ricotta, J., 2009. Abdominal aortic aneurysm risk of rupture: patient-specific FSI simulations using anisotropic model. Journal of Biomechanical Engineering 131, 31001.
Schriefl, A.J., Zeindlinger, G., Pierce, D.M., Regitnig, P., Holzapfel, G.A., 2012. Determination of the layer-specific distributed collagen fibre orientations in human thoracic and abdominal aortas and common iliac arteries. Journal of the Royal Society Interface 9, 1275–1286.
Sgarra, C., Vianello, M., 1997. Rotations which make strain and stress coaxial. Journal of Elasticity 47, 217–224.
Šilhavý, M., 1997. The Mechanics and Thermomechanics of Continuous Media. Texts and Monographs in Physics. Springer.
Spencer, A., 1972. Deformations of Fibre-Reinforced Materials. Oxford University Press.
Spencer, A. (Ed.), 1984. Continuum Theory of the Mechanics of Fibre-Reinforced Composites. CISM Courses and Lectures, vol. 282. Springer.
Spencer, A., Rogers, T., Moss, R., 1974. An optimal angle of winding for pressurized fibre-reinforced cylinders. Mechanics Research Communications 1, 27–32.